EPR as a Tool To Investigate the Transition Metal Chemistry on Oxide Surfaces

Krystyna Dyrek*

Faculty of Chemistry, Jagiellonian University, ul. Ingardena 3, 30-060 Cracow, Poland

Michel Che†

Laboratoire de Réactivité de Surface, URA 1106, CNRS Université P. et M. Curie, 75252 Paris Cedex 05, France

Received July 12, 1995 (Revised Manuscript Received October 25, 1996)

Contents

* Author to whom correspondence should be addressed.
† Institut Universitaire de France.

I. Introduction

The concepts of coordination chemistry, originally established with transition metal complexes in aqueous solutions,[1−7] can be extended to heterogeneous systems consisting of transition metal ions (TMIs) dispersed on the surface of or incorporated into a solid matrix. For such ions, the coordination number, i.e., the number of the donor atoms of the ligands can vary in a large domain. There are important differences in the behavior of TMIs in the bulk of a solid or at the gas (liquid)−solid interface and of their homogeneous counterparts.

In both cases, the coordination of sterically demanding ligands such as polydentate phthalocyanine or Schiff bases in homogeneous complexes or polydentate oxide lattice via rigid O^{2-} ions in heterogeneous systems determines the stereochemistry of the complex. In contrast, small, sterically nondemanding ligands do not influence the coordination of TMIs as much. The phenomena occurring at the gas−solid and liquid−solid interfaces can be also described in terms of coordination chemistry concepts. At the solid surface, the TMI has a lower coordination number than that in the bulk of the solid and may thus complete its coordination sphere by bonding ligands from the gas or liquid phase.

The first coordination sphere predominantly determines the reactivity and properties of the central TMI in both, homo- and heterogeneous systems, but the influence of ligands from the following coordination spheres is much more pronounced in the latter case. This leads to a great variety of TMI complexes in heterogeneous systems and accounts for creation and stabilization at solid surfaces of species with unusual oxidation states, coordination numbers different from those in the bulk of the oxide, and a new type of reactivity, not encountered in homogeneous coordination chemistry. The peculiar features of heterogeneous systems containing TMIs are of special relevance for adsorption and catalysis.

The EPR spectra of TMIs on or in polycrystalline oxides are usually complex, because they often arise from various paramagnetic species. Significant broadening of the spectra, due to the low symmetry of the

S0009-2665(95)00259-7 CCC: $28.00

Krystyna Dyrek received her Ph.D. at the Jagiellonian University, Cracow, Poland, in 1960. She became Professor of Inorganic Chemistry at the same university in 1986. She was a Vice-Rector of the Jagiellonian University in 1990–1993, Vice-Dean of the Faculty of Chemistry in 1984–1990, Head of the Department of Inorganic Chemistry in 1978–1981, and since 1993 she has been again Head of the Inorganic Chemistry Department. Since 1983 she has been a Head of the Research Group of Catalysis and Physico-Chemistry of Solid State. She was Vice-President of the Solid State Chemistry Section of the Polish Chemical Society (1979–1984), Vice-President of the Catalysis Section (1986–1990), and Vice-President of the Inorganic Chemistry Section of this Society. She was invited as a visiting professor to the following universities: Université P. et M. Curie, Paris (since 1983 each year for 1–2 months), the University of Detroit—Mercy (1 month, 1991), University of Bologona (1 month, 1995). Her research areas are physicochemical characterization of heterogeneous catalysts containing transition metal ions dispersed in oxide, aluminosilicate, and polymeric matrices by means of X-ray and electron diffraction, HR TEM/SEM and by spectroscopic methods (EPR, IR, UV–vis, ESCA, etc); spectroscopic studies of the molecular structure and reactivity of surface species; catalytic test reactions of hydrocarbons conversion on redox and acido–basic centers; theoretical and experimental approach to standards for quantitative EPR measurements. She has published over 100 original papers and three review articles (*Appl. Magn. Res.* **1994**, *6*, 309; **1995**, *10*, 319; *Acta Polym.* **1996**, *47*, 1).

M. Che received his Ph.D. at the University of Lyon, France, in 1968. He was Postdoctoral Fellow (1969–1971) at Princeton University. He was attached to CNRS (National Centre of Scientific Research) at the Institute of Catalysis, at Villeurbanne from 1964 to 1975. He then joined the Université P. et M. Curie (Paris) as Director of the Laboratory of Surface Reactivity in 1975 and became Professor in 1976. He was elected President of the Catalysis Division of the French Chemical Society (1989–1994), President-Founder of the European Federation of Catalysis Societies (1990–1995) and Vice-President (1992–1996) and President-Elect (1996 to present) of the Council of the International Congress on Catalysis. He was elected Member of Academia Europaea in 1992, Foreign Member of The Hungarian Academy of Sciences in 1993, and Member of the Institut Universitaire de France in 1995. He was visiting senior scientist (AERE, Harwell, UK) and invited Professor in the People's Republic of China (Academia Sinica), Hungary (Hungarian Academy of Sciences), Japan (Japanese Society for the Promotion of Sciences), and the Republic of China (Chemistry Research Promotion Center). He is honorary Professor at the Universities of Shanxi and Tianjin (People's Republic of China) and guest Professor at the Universities of Pekin and Tai Yuan University of Technology (People's Republic of China). He received several awards (Van't Hoff, The Netherlands; L. Chatin and P. Sue, France). He has given invited and plenary lectures at international conferences, including the 10th Int. Congr. Catal. in 1992, Gordon Conferences in 1988 and 1993, and 2nd Tokyo Conf. Advan. Catal. Sci. Technol. in 1994 and was Distinguished Lecturer in the "Frontiers in Chemical Research" at Texas A&M University in 1995. He was or is member of several Editorial Boards (*J. Chem. Soc., Faraday Trans.*; *Eur. J. Solid State Inorg. Chem.*; *J. Catal.*; *Critical Rev. Surf. Chem.*; *Catal. Rev.*; *Catal. Lett.*; *Top. Catal.; Res. Chem. Interm.*). He is Associate Editor of the Bulletin de la Société Chimique de France. Professor Che works in the field of surface reactivity in relation to adsorption and heterogeneous catalysis phenomena. The main objective is to establish concepts which can help in understanding and predicting activity and selectivity of catalytic materials and in designing more efficient catalysts. The emphasis of his research is on the application of coordination chemistry theories to produce systems with different ion–support interactions. This has led to the emergence of the field of interfacial coordination chemistry and to the use of the so-called chemical glue to prepare supported mono- or bimetallic catalytic materials with a better control of their physicochemical properties.

surface sites and different types of interactions (dipolar, exchange etc.) occurring between the paramagnetic ions, is also a common feature of these systems. Several means can be employed to improve the resolution of powder EPR spectra and to increase the signal to noise ratio, such as registration in a wide range of temperatures, at different microwave power levels and at various frequencies (Q-, K-, X-, L-, S-band), use of isotopes with non-zero nuclear spin, application of thermal and chemical treatments, and accumulation and simulation of the spectra. Usually the best resolved spectra are obtained for isolated TMIs with effective spin $S = {}^1/_2$.

The aim of the present work is to describe the possibilities offered by the joint application of EPR techniques and coordination chemistry concepts to study the molecular structure of transition metal complexes at oxide surfaces and the phenomena occurring at the gas (liquid)−solid interface. Typical examples will be given to illustrate how this approach can improve our understanding of processes related to the preparation of catalysts, adsorption of gases on solid surfaces, chemical reactivity, and catalytic activity of TMIs situated at the gas (liquid)−solid interface.

II. Application of Transition Metal Chemistry Principles to Oxide Surfaces

The principles of coordination chemistry have been established from results obtained essentially by Jørgensen and Werner at the turn of the century on solution complexes containing only one TMI surrounded by ligands.[5,7]

The main goals were to understand the properties of complex salts, i.e., their reactivity toward simple reagents, their structures, the nature of different chemical bonds involved, and the presence and number of geometric as well as optical isomers. Later, attention was focused on their optical and magnetic properties along with their chemical behavior particularly in redox and ligand substitution reactions. Successive theories were proposed (valence bond, crystal field, molecular orbital, angular overlap, etc.) which have greatly helped to improve our understanding of transition metal complexes in solution and inorganic transition metal compounds in the solid state.

Attempts have been made in the past to apply such theories to catalytic systems.[8] It must be recognized that they were by large more successful for homogeneous than for heterogeneous systems, which involve complex gas−solid or liquid−solid interfaces. Substantial progress has now been made for heterogeneous systems, so that a general picture of a field which has been called *interfacial coordination chemistry* (ICC) can be presented. It concerns the preparation of catalysts composed essentially of TMIs and oxide supports, their catalytic properties in the oxidized state, and finally the preparation of supported transition metals. The main results concerning heterogeneous systems include (1) the demonstration that oxide surfaces can be studied, *at a molecular level*, using TMIs as probes, which owing to their partly filled d orbitals lead to characteristic magnetic and optical properties; (2) the demonstration that oxide surfaces may act as σ donor−π donor weak supermolecular ligands and can thus be introduced into the spectrochemical series of ligands; (3) the fact that the oxide support can act as a reactant or a solid solvent; (4) a classification of the different possible coordination chemistries; and (5) the fact that a distinction can now be made between interfacial coordination chemistry and surface organometallic chemistry in the same way as that done for solution complexes.

In what follows, we briefly consider these various points which have been discussed in a recent review in relation to catalysis phenomena.[9]

A. TMIs as Probes of Oxide Surfaces and Interfacial Coordination Chemistry Concepts

In order to probe oxide surfaces, we need to have a suitable *probe*. It is particularly fortunate that TMIs act most often as catalytic sites on an oxide support for they turn out to be also the most appropriate probes to follow their own interaction with the oxide support and *see* the evolution of the catalytic system all along its preparation. Because of their partly filled d orbitals, any change in their first coordination sphere immediately affects their optical and magnetic properties and can thus be detected by spectroscopy. In short, TMIs are both actors and spies watching their own acting.

In order to understand the role of the support, the strategy adopted is to use a *transition metal complex* and investigate how the coordination sphere is modified during the preparation and further post-synthesis treatments.

Because of its pedagogical interest, the competitive ion exchange method has been selected to show that if the adequate parameters of each preparation step are controlled, it becomes possible to obtain the TMI successively (Figure 1) in solution (model I), then *on* (models II−V) and *in* (model VI) the surface, to finally reach the bulk of the oxide (model VII). It is important to stress that models II−V involve TMI in extraframework positions, while models VI and VII concern TMI in framework positions which differ in their accessibility, mobility, and reactivity.[11]

Cation exchange of nickel on silica using nickel nitrate in water−ammonia solution has been studied in detail by UV−vis spectroscopy.[12] In the competitive ion exchange method, the silica surface first comes in contact with an ammonia solution leading to

$$\equiv SiOH + NH_3 \leftrightarrow \{\equiv SiO^-, NH_4^+\} \quad (1)$$

The silica surface then comes in contact with a nickel nitrate solution, giving rise to a competitive ion exchange reaction, where ammonium ions compete with nickel hexaammine complexes to occupy the exchange sites of silica as follows:

$$2\{\equiv SiO^-, NH_4^+\} + [Ni(NH_3)_6]^{2+} \leftrightarrow \{2\equiv SiO^-, [Ni(NH_3)_6]^{2+}\} + 2NH_4^+ \quad (2)$$

The competition level between NH_4^+ and Ni^{2+} ions, expressed as the ratio of their concentrations, allows better control the amount and dispersion of nickel adsorbed.

Reaction 2 indicates that the exchange has occurred and that the oxide surface is acting as a *supramolecular counterion*. Here, the TMI is bonded to the oxide surface by *ligand-screened electrostatic adsorption* (Figure 1, model III).

Upon washing with ammonia solutions, *grafting* occurs via substitution of two NH_3 by two surface $\equiv SiO^-$ ligands according to the scheme

$$\{2\equiv SiO^-, [Ni(NH_3)_6]^{2+}\} \leftrightarrow [Ni(NH_3)_4(\equiv SiO)_2] + 2NH_3 \quad (3)$$

in conditions of pH and NH_3 concentration corresponding to the stability range of the complex $[Ni(NH_3)_4(H_2O)_2]^{2+}$. It is most likely that the grafting reaction actually proceeds via the intermediate tetraammine complex as follows:

$$\{2\equiv SiO^-,[Ni(NH_3)_6]^{2+}\} + 2\ H_2O \leftrightarrow \{2\equiv SiO^-,[Ni(NH_3)_4(H_2O)_2]^{2+}\} + 2\ NH_3 \quad (4)$$

$$\{2\equiv SiO^-, [Ni(NH_3)_4(H_2O)_2]^{2+}\} \leftrightarrow [Ni(NH_3)_4(\equiv SiO)_2] + 2\ H_2O \quad (5)$$

It appears that the ligand exchange NH_3/H_2O in the initial hexaammine complex *weakens* the coordination sphere, making grafting possible via two surface bonds (Figure 1, model IV), with formation of a neutral *cis-octahedral complex*. It is important to note that the oxide, entering into the coordination sphere of Ni^{2+}, becomes a *supramolecular bidentate ligand* via vicinal $\equiv SiO^-$ groups. The latter have been found to be the most probable grafting sites, on the basis of geometrical considerations[12] and by analogy with the silicate structure.[13] This has been confirmed by EXAFS studies.[14]

The *chelating effect of the surface* appears to be the driving force for the formation of the surface cis-octahedral complex. Equation 3, which is the sum of eqs 4 and 5, is accompanied by an entropy increase with the release of water molecules and the disappearance of charged species leading to a subsequent disordering of nearby solvent molecules. This aspect is well-documented in solution coordination chemistry.[5,7]

The previous examples illustrate that the concepts of coordination chemistry can be applied to hetero-

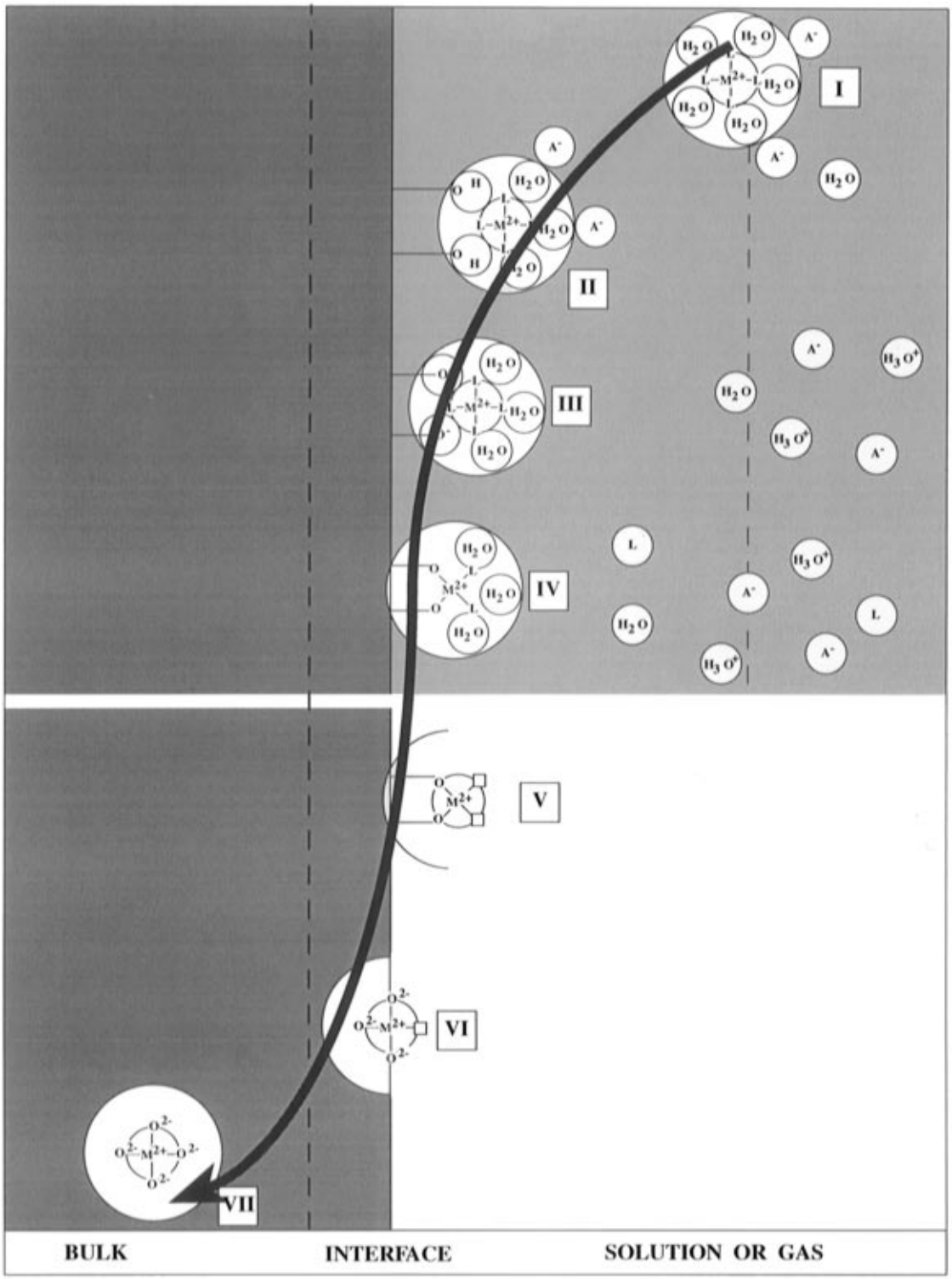

Figure 1. Representation of the outer sphere of solvation and coordination sphere of TMIs at various positions relative to the oxide−fluid (solution or gas) interface. The left-hand side represents the solid oxide. The shaded part on the right-hand side represents the solution while the lower white part on the same side represents the gas.[10] The arrow means that the ion−support interaction increases as one moves from model I to VII.[9]

geneous systems. Once TMIs coming from complexes of the liquid phase (Figure 1, model I) become bonded to the oxide surface (Figure 1, model IV), they can remain attached to the support even though the liquid phase is eliminated and the remaining gas−solid system (Figure 1, model V) heated at higher temperatures. It is then possible to produce vacant coordination sites. The reactivity of such sites toward ligand addition or substitution is the driving force for adsorption and catalysis. This constitutes one of the major differences with coordination compounds in solution. The domain of chemistry which is concerned with the behavior of TMI at solid−fluid (liquid or gas) interfaces is called *interfacial coordination chemistry*.[9]

B. The Supermolecular Ligand Nature of Oxide Surfaces and the Ligand Spectrochemical Series

The inclusion of the oxide surface within the spectrochemical series of ligands is a difficult problem since one is dealing with mixed complexes with

different types of ligands, which each contributes differently to the overall crystal field experienced by the TMI.

The problem can however be solved, providing first the surface complexes along the different preparation steps be prepared and identified and second the *rule of average environment*[15,16] be applied. This rule states that the decrease of the crystal field strength upon substitution of NH_3 by H_2O in the $[Ni(NH_3)_6]^{2+}$ complex is assumed to be a linear function of the number of NH_3 ligands. With ν_3 transition energies of the $[Ni(NH_3)_6]^{2+}$ (28 200 cm^{-1}) and $[Ni(H_2O)_6]^{2+}$ (25 300 cm^{-1}) complexes taken as references,[17,18] a bathochromic $\Delta\nu_3$ shift of -480 cm^{-1} is thus expected for each NH_3 substituted by H_2O.

Since the ν_3 transition of $[Ni(\equiv SiO)_6]^{4-}$ in solution is not available, we have to apply the rule using $[Ni(H_2O)_6]^{2+}$ (25 300 cm^{-1}) and $[Ni(\equiv SiO)_2(H_2O)_4]$ (24 700 cm^{-1}) as references. The latter complex is obtained after reaction of the grafted complex with water written, as follows:

$$[Ni(NH_3)_4(\equiv SiO)_2] + 2H_2O \leftrightarrow [Ni(NH_3)_2(H_2O)_2(\equiv SiO)_2] + 2NH_3 \quad (6)$$

The application of the rule of average environment gives a shift of -300 cm^{-1} for each H_2O molecule replaced by a $\equiv SiO^-$ ligand in the $[Ni(\equiv SiO)_2(H_2O)_4]$ complex. The substitution first of NH_3 by H_2O ($\Delta\nu_3 = -480$ cm^{-1}) and then of H_2O by $\equiv SiO^-$ ($\Delta\nu_3 = -300$ cm^{-1}) gives a total bathochromic shift of -780 cm^{-1} when NH_3 is replaced by $\equiv SiO^-$.

The values derived above allow one to *insert the* $\equiv SiO^-$ *ligand within the spectrochemical series*[19] as follows:

$$I^- < Br^- < S^{2-} < Cl^- < F^- < OH^- < oxalate^{2-} < \equiv SiO^- < H_2O < NH_3 < ethylenediamine < dipyridine < CN^- < CO \quad (7)$$

This order is consistent with theoretical expectations. As a matter of fact, the three ligands, $\equiv SiO^-$, H_2O, and NH_3, are all σ donors. However, it is known from molecular orbital theory that the crystal (ligand) field they can produce is all the more important as their π-donor character decreases.[5,7] This is in good agreement with the presence of two, one, and zero lone pairs on the donor atom for the $\equiv SiO^-$, H_2O, and NH_3 ligands, respectively. The oxalate $C_2O_4^{2-}$ ligand, with two terminal O^- ions, appears to be a very close analogue of the surface bidentate ligand which is a σ donor$-\pi$ donor weak ligand. Similar results are obtained with Cu(II) grafted on pillared clays.[20] The same approach has been taken for other systems such as Pd/SiO_2, Pd/Al_2O_3, and Pd/faujasite-type zeolites using square-planar Pd(II) precursor complexes and led to a *spectrochemical series of supports*.[21]

C. The Oxide Support as a Reactant

A number of papers have reported the presence of intermediate compounds (silicates, aluminates, etc.) after preparation involving the liquid−solid interface, which suggests that the oxide support can act not only as a supermolecular ligand but also as a *reactant* (Figure 1). In the latter case, TMIs are eventually found as framework ions in an intermediate compound represented in the graphical abstract as SOMOSO, etc., where S, O, M stand for the support metal cation, oxide ion, and TMI, respectively.

There are some favorable conditions for the oxide surface to become a reactant. For instance, acidic oxides such as silica are known to dissolve easily in a basic medium.[22] Amphoteric oxides such as alumina, CuO, or ZnO dissolves either in basic or acidic medium, while basic oxides such as NiO dissolve only in acidic medium.[23] The dissolution of the oxide can be regarded as a depolymerization process leading to *support monomers*, which can then copolymerize with the transition metal complexes regarded as *solution monomers*. This copolymerization, particularly for long contact times of the oxide support with the exchange solution, can lead to new phases such as nickel silicates for the Ni/SiO_2 system.[24]

It is thus important to understand how bond formation occurs between *molecular* solution species. Sol−gel processes indicate that there are some preferred pathways such as

$$M-OH + M-H_2O \leftrightarrow M-OH-M + H_2O \quad (8)$$

$$M-OH + M-OH \leftrightarrow M-O-M + H_2O \quad (9)$$

where M represents the support ion and/or any TMI.

Olation (reaction 8) and *oxolation* (reaction 9) are condensation processes in which a *hydroxy* or an *oxo bridge* between two metal centers are formed respectively.[25] It becomes clear now that if H_2O, OH^-, or O^{2-}, which all are bridging ligands, are substituted by nonbridging ones such as NH_3 around the TMI, bond formation between the two metal centers will be inhibited. When oxide supports are involved, intermediate compounds can be formed on the surface of oxide supports. In such cases the species corresponding to reactions 8 and 9 can have M in either framework or extraframework positions.

D. The Oxide Support as a Solid Solvent

TMIs can be found as framework ions (Figure 1, models VI and VII) using other preparation methods. For instance, one involves thermal pretreatments of systems with extraframework ions deposited by methods such as competitive ion exchange seen above or simple impregnation method. For instance, when V_2O_5 is deposited by impregnation on TiO_2 and the system obtained is heated thermally, ion migration occurs and V^{4+} ions can be observed by EPR in framework positions.[26]

The oxide can also act as a *solid solvent* as in the case of oxide solid solutions directly prepared as such, by coprecipitation. The coprecipitation in a precursor form (hydroxides, carbonates, etc.) of both the support and the active phase from a solution has the advantage of producing an intimate mix. The coprecipitate leads on calcination to a support with the active component dispersed throughout the bulk as well as at the surface. The support can thus be considered as a *solid solvent*. The ideal case is obtained for systems such as NiO−MgO or CoO−MgO, where the MgO host matrix of rock-salt structure acts also as a *sterically demanding polydentate ligand*.[11] Depending on the location of theTMI, the oxide can act

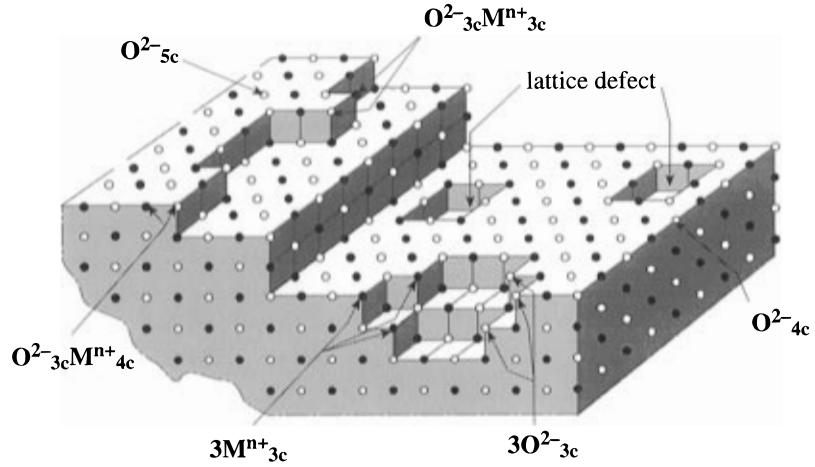

Figure 2. Representation of a surface (100) plane of MgO showing surface imperfections such as steps, kinks, corners, etc., which provide sites for M_{lc}^{n+} and O_{lc}^{2-} ions of low coordination (lc = 3c, 4c, 5c). M^{n+} ions can be either Mg^{2+} or TMIs such as Co^{2+}, Ni^{2+}, etc.[9]

as either a penta-, tetra-, or terdentate sterically demanding ligand (Figure 2).

The TMI, now in surface framework position (Figure 1, model VI), is all the less likely to change its coordination with the rigid surface ligand as its coordination number is important. In Figure 2, the same notation has been adopted for O^{2-} [27,28] and TMIs[29,30] in positions of *low coordination* and can be easily extended to other types of ions, provided the coordination number is known. The reactivity of ions in framework positions and at the oxide surfaces has been studied in detail. This has been done by EPR and IR for Co^{2+} ions of CoO−MgO solid solutions toward natural molecular oxygen or enriched in ^{17}O.[31,32] The domain of chemistry which is concerned with the behavior of TMIs in framework positions at oxide surfaces is called *surface solid state chemistry*.[9]

E. A Classification of the Different Possible Coordination Chemistries

As shown above, the two domains of interfacial coordination chemistry and surface solid state chemistry have distinct characteristics with the oxide surface acting essentially as supramolecular ligand and reactant (or solid solvent) respectively.

On the basis of the models given in Figure 1 and of the results given in sections A−D, it is possible to propose a simple classification of the different types of coordination chemistries related to systems involving TMIs and oxide supports. This classification[10] can be easily extended to other supports (sulfides in particular).

Interfacial coordination chemistry is clearly *intermediate* between solution (Figure 1, model I) and solid state (Figure 1, model VII) coordination chemistries. It can be subdivided into two coordination chemistries referring to ions in extraframework positions (Figure 1, models II−V) on the one hand and the surface ions in framework positions (Figure 1, model VI, and Figure 2), on the other hand. Whereas the reactivity of the former ions depends on the gas-phase pressure in the former case, it essentially depends for the latter on the location of the ions at the surface. In following the arrow in Figure 1, the reactivity, mobility, and accessibility of the TMIs continously decrease in contrast with ion−support interactions, which continously increase. Concerning the mobility and as pointed out earlier,[33] the zeolites present such a structure that ions can move from hidden sites to large cavities on adsorption of polar molecules. The interface can now be defined, from the standpoint of the probe, as the *intermediate region* where there is a *transition* from the properties of TMIs in solution to those in the solid state: it extends from 8−10 water layers, on the liquid side,[9] to a depth, on the solid side, equivalent to the radius of the TMI solvation sphere (see Figure 1). The importance of the interface has already been pointed out by Haber.[34]

F. Interfacial Coordination Chemistry and Surface Organometallic Chemistry

The above examples have shown that complex systems such as oxide-supported TMIs can nevertheless be treated as classical coordination compounds, where the oxide surface can simply be regarded as a supermolecular mono- or polydentate ligand, able to bind a substantial number of TMIs separately (isolated ions) or together (oligomers or oxide particles).[35] Table 1 summarizes the distinction which may be

Table 1. Comparison of the Main Characteristics and Applications of the Two Domains of Interfacial Coordination Chemistry (ICC) and Surface Organometallic Chemistry (SOMC)

	ICC	SOMC
metal oxidation state	high	low
ligands	hard (Pearsons); σ donor (π donor); S^{2-}, Cl^-, O^{2-}, H_2O, NH_3	soft (Pearsons); σ donor - π acceptor; CO, PR_3, organic ligands
M−L interactions	more ionic	more covalent
models	crystal field; molecular orbitals	molecular orbitals; $18e^-$ stability rule; $16-18e^-$ reactivity rule
applications	ligands slightly perturbed; catalyst preparation; selective ion adsorption	ligands perturbed; organic synthesis; catalysis

proposed between interfacial coordination chemistry (ICC) and surface organometallic chemistry (SOMC). It gives the main characteristics of these two fields and stresses the main domains of application. This classification should be used only as a guide and not taken too literally.

III. Model EPR Spectra of Polycrystalline Samples

The oxide samples containing TMIs are usually polycrystalline materials, composed of numerous small crystallites randomly oriented in space. The resultant EPR spectrum is the envelope of elementary resonance lines corresponding to all possible orientations of the small crystallites containing the paramagnetic species with respect to the magnetic field. The **g** tensor ellipsoid with principal values ($\mathbf{g}_{xx}$, $\mathbf{g}_{yy}$, $\mathbf{g}_{zz}$) along the *x*, *y*, and *z* principal axes with respect to which the orientation of the applied magnetic field can be defined by the angles θ and ϕ is presented in Figure 3. The profile of a powder spectrum is determined by several parameters among which the most important are the symmetry of the **g** and **A** tensors, the values of their components, and the line width. Provided the spectra are well resolved and there is no overlapping of different signals, the **g** tensor components ($\mathbf{g}_{iso}$; $\mathbf{g}_{\perp}$, $\mathbf{g}_{||}$; $\mathbf{g}_{xx}$, $\mathbf{g}_{yy}$, $\mathbf{g}_{zz}$) can usually be determined from inflection points of the experimental spectra (vide infra).

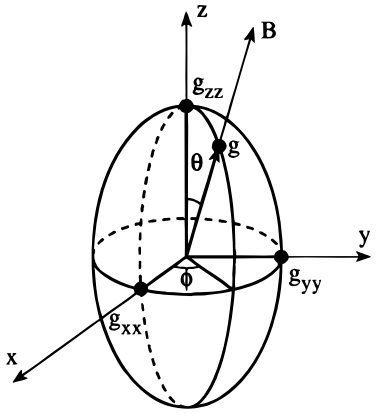

Figure 3. Orientation of the magnetic field **B** with respect to the g tensor ellipsoid in the frame of *x*, *y*, *z* principal axes. θ and ϕ are the characteristic angles defining the orientation of **B** and leading to the $\mathbf{g}(\theta,\phi)$.

A. EPR Spectra Characterized by the g Tensor Alone

This is the case where all surrounding atoms or ions have nuclei with $\mathbf{I} = 0$. The factor decisive about the signal profile is then the **g** tensor symmetry. The **g** tensor may be isotropic, axial, or orthorhombic.

The isotropic EPR lines with $\mathbf{g}_{xx} = \mathbf{g}_{yy} = \mathbf{g}_{zz} = \mathbf{g}_{iso}$ are not very often observed in the case of polycrystalline samples except for some solid-state defects and TMIs in highly symmetric environment. An apparent isotropy may be encountered in low viscosity solutions where, whatever the symmetry of the **g** tensor, a radical is subjected to very rapid tumbling and reorientation. The observed **g** value becomes the time average of the three components:

$$\mathbf{g}_{av} = (\mathbf{g}_{xx} + \mathbf{g}_{yy} + \mathbf{g}_{zz})/3 \qquad (10)$$

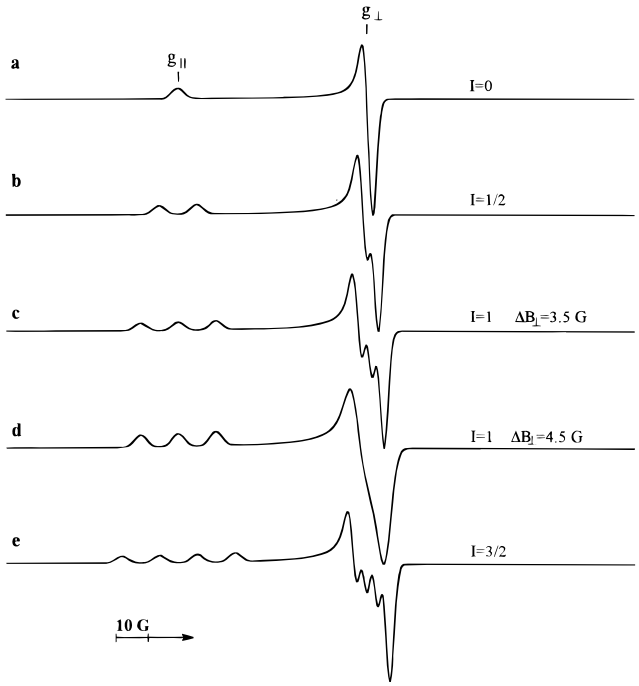

Figure 4. Calculated EPR spectra for species with $S = {}^1/_2$ and axial **g** tensor in presence of single nucleus with nuclear spin *I*. Figure d shows the effect of broadening of the signal c on the resolution of the spectrum.

More common are the EPR spectra of polycrystalline samples with axial symmetry. Figure 4a gives a schematic representation of the first derivative signal, for a polycrystalline sample with a paramagnetic center in axial symmetry.

Assuming that the microcrystals in a powder sample are randomly distributed in space, simple considerations[36] show that the absorption intensity, which is proportional to the number of microcrystals at resonance for a given θ value, is maximum when $\theta = \pi/2$ and minimum for $\theta = 0$ at magnetic field values $\mathbf{B}_{\perp}$ and $\mathbf{B}_{||}$, respectively; this allows the extraction of the $\mathbf{g}_{\perp}$ and $\mathbf{g}_{||}$ values which for sharp signals practically correspond to the turning points of the spectrum in Figure 4a.

The actual width of the lines strongly influences the spectral profile and the resolution. The latter becomes very poor for increasing line width as seen by comparison of Figures 4c and 4d.

In the case of orthorhombic symmetry, the EPR first derivative of the absorption line exhibits three singular points corresponding approximatively to $\mathbf{g}_1$, $\mathbf{g}_2$, and $\mathbf{g}_3$[36] (Figure 5a). The approximation is satisfactory only for very narrow signals. For powder spectra, the assignment of $\mathbf{g}_1$, $\mathbf{g}_2$, and $\mathbf{g}_3$ to the principal components $\mathbf{g}_{xx}$, $\mathbf{g}_{yy}$, and $\mathbf{g}_{zz}$ of the paramagnetic center is not straightforward and must be based on theoretical grounds or deduced from measurements of the same paramagnetic species in single crystals where the crystal axes can be conveniently oriented with respect to the external magnetic field.

B. EPR Spectra Characterized by the g and A Tensors Together

The situation becomes much more complicated in the case of the combined effect of the **g** tensor anisotropy and the hyperfine (hf) splitting due to the interaction of unpaired electron with nucleus of the

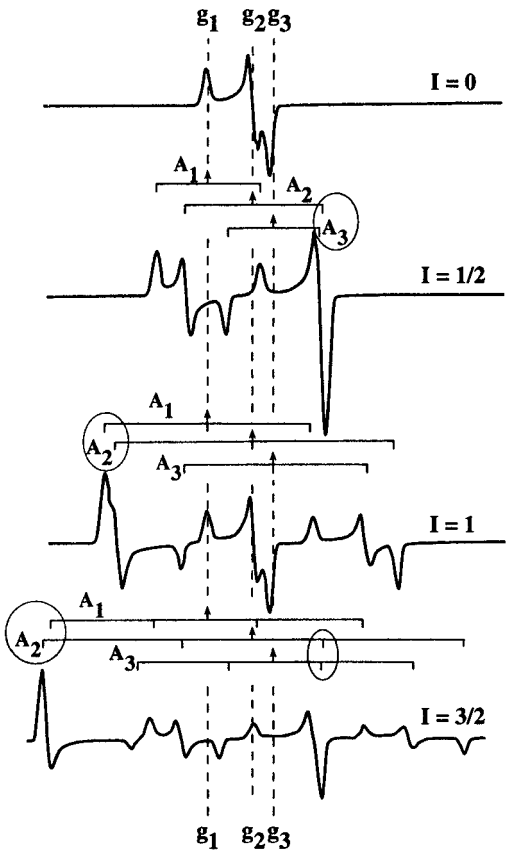

Figure 5. Effect of the presence of one nucleus with nuclear spin I on the calculated EPR spectra of an orthorhombic species with various sets of hyperfine constants. The number of hyperfine lines centered on each **g** tensor component is given by $2nI + 1$ ($n = 1$ here and I takes values 0, $^1/_2$, 1, $^3/_2$). Note overlapping of hyperfine components shown in the figure by circles. (Adapted from ref 37.)

same paramagnetic ion, providing that its nuclear spin $I \neq 0$.[37] Then each of the three lines of the **g** tensor ($\mathbf{g}_1$, $\mathbf{g}_2$, $\mathbf{g}_3$) will be split into a number of lines ($2nI + 1$), depending on the number n of equivalent nuclei involved and the value of the nuclear spin I. The spacing between the hf lines will correspond to the appropriate components of the **A** tensor ($\mathbf{A}_1$, $\mathbf{A}_2$, $\mathbf{A}_3$) with $\mathbf{g}_1$ split by $\mathbf{A}_1$, $\mathbf{g}_2$ by $\mathbf{A}_2$ and $\mathbf{g}_3$ by $\mathbf{A}_3$.

The number of distinct cases derived from the different possibilities of combining the anisotropies of both **g** and **A** tensors is very high and cannot be easily summarized. Some particular examples are thus given in Figures 4 and 5[37] which have been obtained by calculating the spectral profile by means of the simulation program SIM 14A.[38] In Figure 5, the effect of the nuclear spin on the orthorhombic spectrum anisotropic both in **g** and **A** tensors is reported. The first spectrum ($I = 0$, no hf structure) exhibits well-separated $\mathbf{g}_1$, $\mathbf{g}_2$, and $\mathbf{g}_3$ features which are split in the successive spectra when the hf interaction is considered and values for I (from $^1/_2$ to $^3/_2$) and $\mathbf{A}_1$, $\mathbf{A}_2$, and $\mathbf{A}_3$ are introduced in the computation. For the sake of simplicity, the abundance for the $I \neq 0$ nucleus has been considered to be 100%.

When I takes an integer value, the features of the original $I = 0$ spectrum are maintained at the center of the spectrum while when I is a half-integer the hf lines dispose symmetrically about the center where no such $I = 0$ spectrum is observed. Obviously, the complexity of the spectra and the number of lines increase with increasing I values. It must be noticed that in some instances, the hf lines related to different components of the **A** tensor lie very close one to the other leading to overlap and possible ambiguities in the assignment (Figure 5).

Many systems in addition to the hf structure show a splitting due to the interaction of unpaired electron of the central atom with ligand nuclei ($I \neq 0$) or unpaired electron of the ligand with the metal nuclei ($I \neq 0$). This splitting leads to the so-called superhyperfine (shf) structure which is observed when covalent bonding exists between the metal atom and the ligand orbitals. The examples of the shf structure are given in sections V.B.2 and V.E.2.

IV. The Working Tools To Extract Magnetic Parameters from Experimental Powder EPR Spectra

In this section, we will give indications on how to resolve powder EPR spectra and what kinds of information can be derived from spin Hamiltonian parameters which can be useful in solving coordination chemistry problems on oxide surfaces.

Very often, in real solid samples, several paramagnetic species are present and their signals can overlap to give a broad, poorly resolved spectrum. The main task of the experimentalist consists of (1) separating the particular component signals contributing to the overall spectrum; (2) assigning the individual signals to a given paramagnetic species; and (3) confirming the assignment by simulation and theoretical calculations.

Various means (physical, chemical, and numerical) can be employed to achieve this goal.

A. Deconvolution of Complex EPR Spectra into Component Signals

The deconvolution may be based on various properties of the paramagnetic centers depending on their (1) location at the surface or in the bulk of the oxide support, (2) different properties such as saturation ability, relaxation characteristics, and chemical reactivity.

1. Physical Tools

a. Registration of the Signal at Various Power Levels and/or Different Temperatures. This method consists of the separation of the components of the spectrum on the basis of different saturation abilities. The species with long relaxation times T_1 and T_2 become easily saturated, i.e., their Zeeman levels become equally populated and no EPR transition can occur. This is the case of organic radicals and solid-state defects weakly coupled to the lattice. These easily saturating species can be eliminated from the spectra by increasing power of the microwave radiation.

The spin−lattice (T_1) and spin−spin (T_2) relaxation times of TMIs are usually short enough to avoid saturation, in the temperature range commonly used (77 K to room temperature) to register the spectra. The paramagnetic species containing TMIs differ

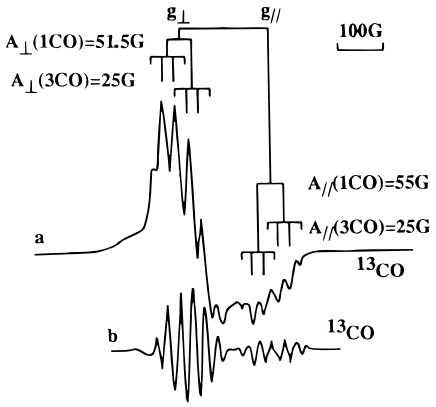

Figure 6. EPR spectra (X-band, 77 K) after adsorption of ^{13}C-enriched CO under a pressure of 400 torr on silica supported Ni^{+} catalysts: (a) first derivative and (b) third derivative.[39]

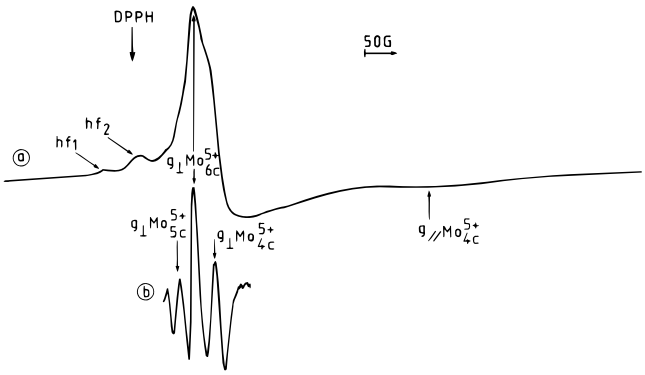

Figure 7. EPR spectrum (X-band, 77 K) of a reduced grafted Mo/SiO_2 catalyst: (a) first derivative and (b) third derivative. (Reprinted from ref 40. Copyright 1987 American Chemical Society.)

however in their relaxation time which causes different dependence of the signal intensity on temperature.

Thus, measuring of the intensity of particular components of the spectrum as a function of temperature and power level allows one to distinguish signals originating from various species.

b. Third Derivative Presentation. In the case of broad, overlapping signals, a useful approach for spectra resolution consists in recording, besides the conventional first derivative, the third derivative spectra. The enhancement in resolution is clearly seen, e.g., in the spectrum of Ni^{+} tetracarbonyl complex obtained after adsorption of ^{13}C-enriched CO under 400 Torr on the surface of Ni^{+} containing Ni/SiO_2 catalysts[39] (Figure 6). Ni^{+} ions were created by slight thermal reduction of Ni^{2+} supported on SiO_2, in hydrogen at 443 K.

Another example is given by silica-supported molybdenum catalysts obtained by the grafting method,[40] leading, after reduction in hydrogen at elevated temperature, to a broad signal which in the third derivative presentation exhibits three lines corresponding to three different Mo^{5+} species (Figure 7) (see also sections IV.D. and V.B.1).

c. Multifrequency Approach. Sometimes it is difficult to distinguish between the patterns arising from **g** tensor anisotropy or hf splitting. Recording the spectra at more than one microwave frequency may help in solving this problem. The principle of the method is based on the fact that the separation

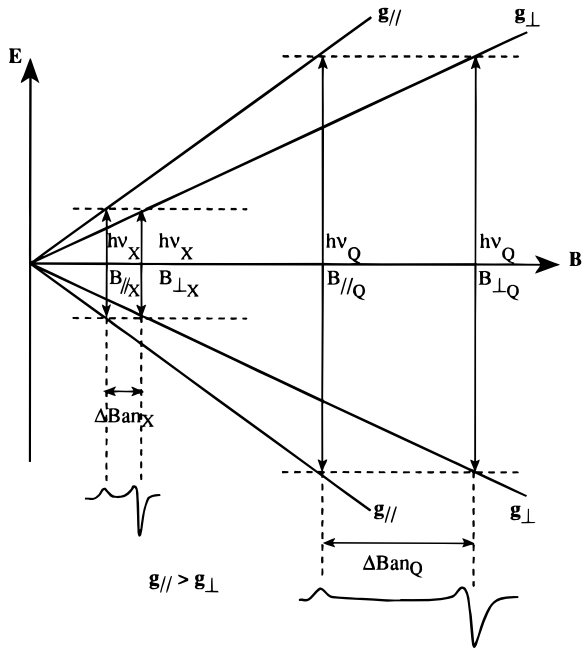

Figure 8. Field separation between the principal **g** values in X- and Q-band in the case of axial symmetry and $\mathbf{g}_{\|} > \mathbf{g}_{\perp}$. (Reprinted from ref 41. Copyright 1994 Plenum Press.)

ΔB_{an} between the signal components related to the **g** tensor anisotropy varies linearly with the microwave frequency according to the equation:

$$|\Delta B_{an}| = h\nu/\mu_B|(1/\mathbf{g}_1) - (1/\mathbf{g}_2)| \qquad (11)$$

The way of measuring the field separation ΔB_{an} between the principal **g** values ($\mathbf{g}_{\perp}$, $\mathbf{g}_{\|}$) of a species with axial symmetry in X-band ($\nu = 9.5$ GHz) and Q-band ($\nu = 35$ GHz)[41] is presented in Figure 8. The spacing between $\mathbf{g}_{\perp}$ and $\mathbf{g}_{\|}$ increases in the ratio of the frequencies, i.e., by a factor of about 4 on going from X- to Q-band.

The multifrequency approach enables distinction between the tensor **g** components and features arising from hf [superhyperfine (shf)] interaction, since the **A** tensor features are unaffected to first order by microwave frequency changes.

This approach has been taken by Lunsford and Vansant[42] in the case of hexacoordinated low-spin d^7 complex of Co^{2+} in Y zeolite (Figure 9). Two sets of eight lines, separated by 67 and 72 G, respectively, are observed in the EPR spectrum of Co^{2+} in both, X- and Q-band (Table 2, A-3,5,6). (For a description of Table 2, see section V.) The same separation of the lines at both frequencies indicates that their origin comes from hf interaction while the presence of two sets of hf lines indicates the axial symmetry of the **g** tensor.

It should be noticed that for polycrystalline materials with a broad range of sites at which paramagnetic centers are located, this approach may sometimes fail. This is the case of Mo^{5+} in ^{95}Mo-enriched Mo/SiO_2 catalysts obtained by impregnation method[43] and reduced in hydrogen at 500 °C, which in Q-band gives a broad unresolved line (Figure 10) although in the lower frequency X-band a well resolved spectrum with hf structure is observed (see Figure 14b in section IV.A.2). (Table 2, K-12). It has been shown,[44] that the individual line width ΔB depends

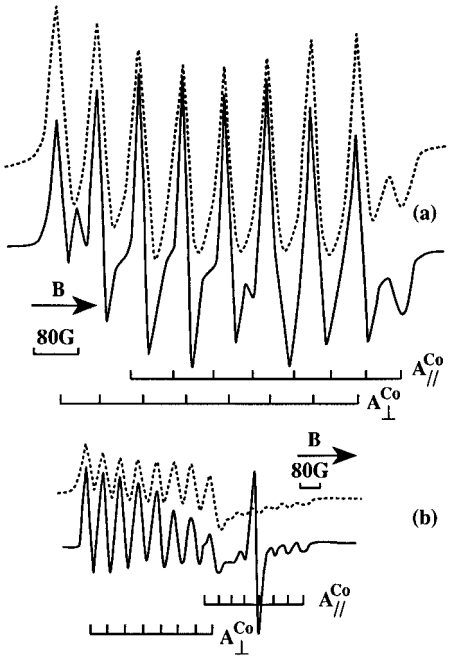

Figure 9. Experimental (solid line) and simulated (dotted line) EPR spectrum (77 K) of $[Co(CH_3CN)_6]^{2+}$ in the X-band (a) and Q-band (b). (The isotropic line at the center of the parallel structure is due to another species.) (Reprinted from ref 42. Copyright 1973. Chemical Society of London.)

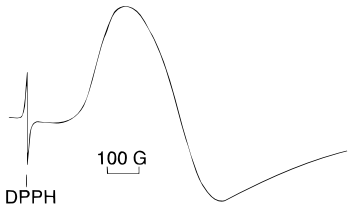

Figure 10. EPR spectrum (Q-band, 300 K) of a ^{95}Mo-enriched Mo/SiO_2 catalyst reduced by hydrogen at 500 °C. (Reprinted from ref 43. Copyright 1978 Chemical Society of London.)

on the angle θ [between the magnetic field and the principal axis taken as the z axis (Figure 3)] and the resonance frequency ν as

$$\Delta B(\theta,\nu) = 2h/\mu_B \cdot \mathbf{g}^{-2}(\theta)\, \delta\mathbf{g}(\theta)\nu \qquad (12)$$

This relation shows that the disappearance of the hf lines due to ^{95}Mo nuclei ($I = {}^5/_2$) in the Q-band spectrum (compare Figures 10 and 14b) is caused by the increase, particularly at high frequency, of the individual line width due to the distribution of the Mo^{5+} sites, i.e., distribution of the **g** components.

In recent years it became evident that microwave frequencies lower than 9 GHz (X-band) are particularly useful in studies of disordered systems where local structural inhomogeneities ("strains") lead to a distribution of the **g** and hf tensors and cause considerable line broadening.[45] In order to find optimum resolution it may be necessary to investigate the system over a continous range of frequencies between about 1 and 35 GHz.

A model that describes the line widths in the EPR spectra of Cu^{2+} complexes as a function of microwave frequency and m_I values was elaborated by Froncisz and Hyde.[46] The distribution widths of the parallel component of the **g** tensor and of the hf tensor from

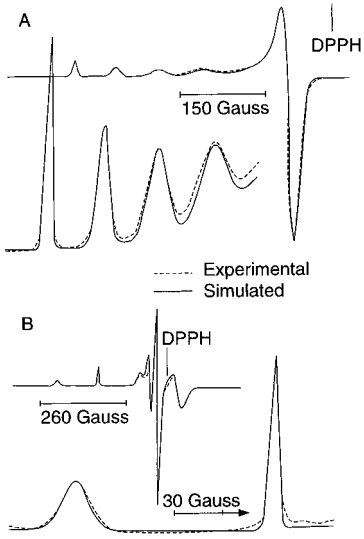

Figure 11. Simulated (solid line) and experimental (dotted line) ESR spectra of Nafion $^{63}Cu^{2+}$ D_2O (Cu^{2+} content 1%): (A) X-band, 100 K, $\nu = 9.376$ GHz; (B) S-band, 123 K, $\nu = 2.359$ GHz. (Reprinted from ref 47. Copyright 1993 Elsevier.)

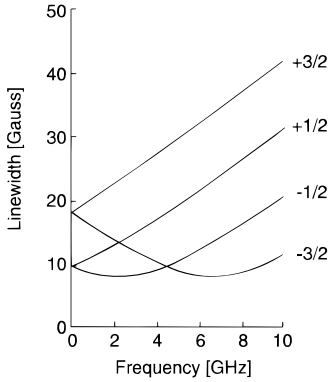

Figure 12. Variation of the line width from the four signals of the parallel transition as a function of the microwave frequency. (Reprinted from ref 47. Copyright 1993 Elsevier.)

the central cation, $\delta\mathbf{g}$ and $\delta\mathbf{A}$, respectively, can be deduced from experimental spectra using this model.

The effect of microwave frequency on EPR spectra of Cu^{2+}coordinated by oxygens in Nafion membrane swollen by D_2O was studied by Schlick and coworkers[47] in L- (1.25 GHz), S- (2.36 GHz), and X- (9.38 GHz) bands. Figure 11 represents experimental and simulated spectra at two frequencies (X- and S-band) while in Figure 12 the line widths of the parallel signals are plotted as a function of microwave frequency for the four m_I values of the parallel component. It is seen that for $m_I = -{}^1/_2$ the narrowest line can be detected around $\nu = 2$ GHz, as expected from the already mentioned model, while for $m_I = -{}^3/_2$ the narrowest line is measured at 7 GHz. Frequencies higher than 9 GHz cause significant broadening and are not useful in the investigated system.

2. Chemical Tools

a. Testing the Oxide Surface with Probe Molecules. This method consists of using probe molecules to test various features of oxide surfaces. An extensive review on this topic was recently published.[37] Different effects are observed, e.g.

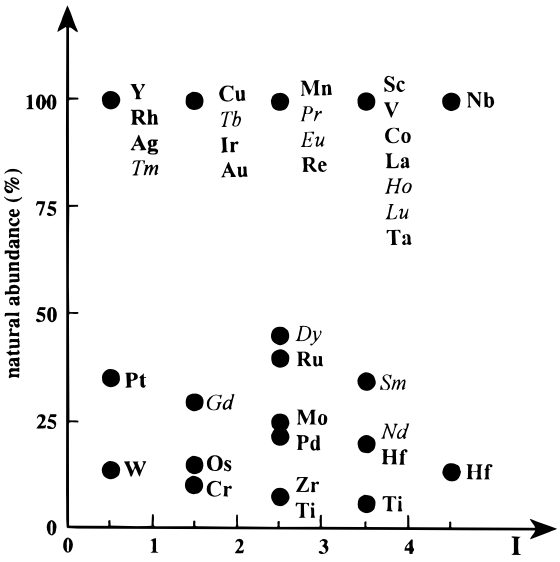

Figure 13. The most abundant isotopes of d (**bold characters**) and f elements (*italics*) with $I \neq 0$ nuclear spin. For the same I and abundance, the ordering of the elements corresponds to increasing atomic number Z. For elements having more than one isotope with the same nuclear spin value (I), points (·) in the figure correspond to the sum of abundancies. (Data from Table 1 in ref 48.)

changes in the line shape, line width, and **g** values, depending on the type and strength of interaction of the probe molecule with the paramagnetic centers on the oxide surface. Physical interactions, e.g. magnetic dipole−dipole interactions, cause usually reversible (vanishing upon outgassing) broadening of EPR signals of paramagnetic surface species upon interaction with paramagnetic probe molecules, like O_2. This method is commonly used to distinguish between the species situated in the bulk and on the surface of oxides. Chemical interactions not accompanied by an electron (proton, etc.) transfer change the coordination number of the surface complex without changing oxidation state of the central atom or ligands (see sections IV.D, VB.1, V.B.2, V.E.1). Examples of using probe molecules to determine the oxidation state of a TMI without changing its value are given in section V.A.1. Chemical interactions occurring with electron transfer may be used to test redox properties of the oxide surfaces with electron donor (acceptor) probe molecules (see V.E.2).

b. Isotopic Labeling. This method is used to produce a hf or shf structure, i.e., when the investigated sample does not contain isotopes with nuclear spin $I \neq 0$ or when the natural abundance of such isotopes is small. The values of the $I \neq 0$ nuclear spins of the most abundant isotopes of transition metals are presented in Figure 13.

The hf or shf patterns differ strongly for elements with different I values and abundances. Even in the case of the same I value and abundance, distinguishing between the hf patterns is possible on the basis of hf (shf) coupling constants which are related to the values of nuclear magnetic moments.[48]

The effect of isotopic labeling may be illustrated by reduced impregnated Mo/SiO_2 catalysts[43] (see also previous section). A large EPR signal was observed at 77 and 293 K, with $\mathbf{g}_\perp = 1.940$ and $\mathbf{g}_\parallel = 1.882$, characteristic of Mo^{5+} in an axial crystal field (Figure

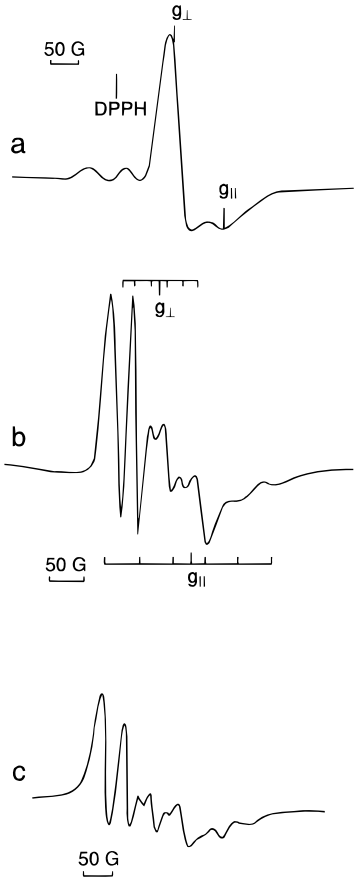

Figure 14. EPR spectra (X-band, 300 K) of a Mo/SiO_2 catalyst reduced by hydrogen at 500 °C: (a) natural abundance of ^{95}Mo isotope ($I = {}^5/_2$, ~25%), (b) catalyst enriched in ^{95}Mo isotope (97%), (c) simulated spectrum with magnetic parameters deduced from the spectrum b. (Reprinted from ref 43. Copyright 1978 Chemical Society of London.)

14a). On the low-field side of the spectrum two small peaks were detected which changed with temperature and microwave power in the same way as the main anisotropic signal, indicating that they are part of the same spectrum. These two peaks were considered as components of the hf structure. Molybdenum possesses only two isotopes with nuclear spin $I \neq 0$, ^{95}Mo and ^{97}Mo, of natural abundances 15.78 and 9.60%, respectively (Figure 13). Both isotopes have the same nuclear spin $I = {}^5/_2$ and about the same magnetic moment (−0.9270 and −0.9485 μ_N, respectively[48]) so that the hf structures resulting from each are largely superimposed. The resulting EPR spectrum would consist of six equally spaced hf lines centered about the parallel and perpendicular features arising from the isotopes with $I = 0$. The hf lines should have a relative intensity ~6% of the main feature (parallel or perpendicular) with which they are associated. In the spectrum of Mo/SiO_2 catalysts, the observed ~6% relative intensities ratio of the two low field lines with respect to the perpendicular line suggests that they belong to the perpendicular hf pattern. The parallel hf lines are not seen.

This assignment is confirmed by the use of catalysts enriched in ^{95}Mo isotope (97% enrichment). Figure 14b represents the EPR signal of the reduced $^{95}Mo/SiO_2$ system where not only the perpendicular but also the parallel hf pattern are seen. The change in the EPR spectrum on labeling with ^{95}Mo shows

unambiguously that the corresponding paramagnetic species is associated with molybdenum ions. The simulation of the spectrum presented in Figure 14c confirms such assignment (Table 2, A-3,5,6). (For a description of Table 2, see section V.)

In view of the variety of informations which may be obtained from the hf and shf patterns (vide infra), the relevance of the method of isotopic labeling is evident.

c. Chemical Treatment. The chemical treatment, e.g. oxidation or reduction at various temperatures and pressures, may be used to eliminate some of the species contributing to the complex spectrum and to enhance the concentration of others. This procedure was successfully applied to identify the different molybdenum species in reduced MoO_3.[49]

B. Identification of Paramagnetic Centers in Real Solid Systems

The identification of particular paramagnetic species extracted from the complex spectrum is mainly based on the analysis of **g** and **A** tensor values.

1. Identification from the g Tensor

Only in a limited number of cases, the values of the **g** tensor alone allow one to identify the paramagnetic ion. Even in the case of typical **g** values, e.g., of d^9 ions (Cu^{2+}, Ni^{+}), additional information such as hf and shf parameters are necessary to attribute the observed EPR signal to a given paramagnetic species.

2. Identification from the hf and shf Tensors

As described earlier (section III.B), the information which can be obtained from the hf (shf) pattern is derived from the number of lines, their relative intensities, and the number and values of **A** tensor components.

Examples illustrating the use of hf (shf) structures to identify the species involved in hf (shf) interaction are given in sections IV.A.2, V.A.1, and V.B.2.

C. Spectra Simulation

Numerical methods are commonly used for EPR data acquisition, processing, and evaluation. The spin Hamiltonian parameters obtained from the experimental spectrum can be further refined by computer simulation. The simulation leads to accurate values of the magnetic parameters for each species contributing to the spectrum and provides information on their relative populations (see, e.g., Figures 14c and 16).

D. Quantitative Approach

The quantitative approach to EPR spectra is based on the direct proportionality between absorbed microwave energy and the number of paramagnetic species taking part in the resonance. The most common method of spin dosimetry consists of comparing the EPR signal intensity of an unknown sample with that of a standard with a known spin concentration. This approach requires a very precise control of the factors influencing the EPR signal intensity.[50]

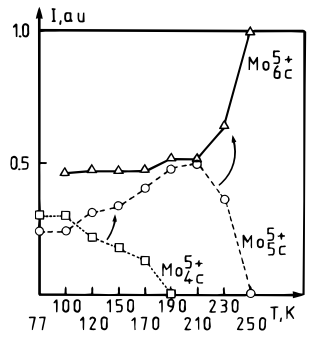

Figure 15. Plots of the EPR signal intensity (measured as the height of $\mathbf{g}_\perp$ component) of Mo_{4c}^{5+}, Mo_{5c}^{5+}, Mo_{6c}^{5+} species as a function of temperature after methanol adsorption at 77 K on reduced Mo/SiO_2 catalyst. (Reprinted from ref 58. Copyright 1991 Polish Academy of Sciences.)

The experimental parameters (receiver gain, modulation amplitude, incident microwave power, filling factor, temperature, etc.), for the investigated sample and the reference, should be the same or be changed by a known factor.

Advanced chemical methods are applied to prepare the standard samples and to determine the concentration of paramagnetic centers by chemical analysis. The appropriate standard for quantitative EPR measurements should be at the best, similar—as far as possible—to the investigated sample with respect to the electronic structure of the paramagnetic centers, symmetry of their surroundings, nature of ligands, spin concentration, etc. Statistical methods are used for evaluating the quality of standards.[51]

The reference materials commonly used for spin dosimetry are listed by Chang in a review article.[52] The procedure of preparation of standards based on vanadyl sulfate for quantitative EPR measurements of d^1 TMIs is described in ref 51.

Numerous examples can be given to illustrate the importance of the quantitative determination of the number of spins in interface studies (Table 2, E-11), e.g., the mechanism of propylene adsorption on MoO_3 was deduced from the changes of Mo(V) signal intensity as a function of temperature and pressure.[53] The kinetic model of redox processes occurring in V_2O_5/MoO_3 catalysts upon interaction with oxygen and propylene was elaborated on the basis of quantitative EPR measurements.[54−56] Two different centers of reduced vanadium, stabilized by oxygen vacancies or by Mo(VI) ions, were identified.[55,56]

Another example is the quantitative determination of isolated Co(II) ions in CoO-MgO solid solutions, which revealed a strong correlation between the number of these ions and the amount of oxygen adsorbed as O_2^- radicals.[57]

In certain cases, when the line shape remains unchanged even a simple method of measuring the height of the signal gives valuable results. For instance, Figure 15 represents changes in the EPR signal intensities of three molybdenum species: Mo_{4c}^{5+}, Mo_{5c}^{5+}, and Mo_{6c}^{5+} as a function of temperature after methanol adsorption on reduced grafted Mo/SiO_2 catalyst at 77K[58] (see also sections V.B.1 and V.E.1) (Table 2, F-14). The signal of reduced Mo/SiO_2 sample was given in Figure 7. The assignment of the broad first derivative signal (Figure 7a) to three Mo^{5+} species with different coordination numbers, four (species Mo_{4c}^{5+} with $\mathbf{g}_\perp = 1.926$ and $\mathbf{g}_\parallel = 1.755$),

five (species Mo_{5c}^{5+} with $\mathbf{g}_\perp = 1.957$ and $\mathbf{g}_\parallel = 1.866$), and six (species Mo_{6c}^{5+} with $\mathbf{g}_\perp = 1.944$ and $\mathbf{g}_\parallel = 1.892$), respectively, was based on the analysis of **g** tensor components derived from the complex EPR spectrum by means of the third derivative presentation (Figure 7b), on the behavior of the spectrum at different temperatures and frequencies and upon adsorption of probe molecules at various pressures[40] (Table 2, F-1,2,13,14).

After methanol adsorption at temperatures below 100 K, all three Mo^{5+} species were present in comparable amounts, while above 200 K the hexacoordinated Mo_{6c}^{5+} increased strongly, first, at the expense of Mo_{4c}^{5+} and then at the expense of Mo_{5c}^{5+} (Figure 15). During this process, the integral intensity of the overall spectrum remained constant which indicates that the transformation of the surface complexes of Mo^{5+} occurs via coordination of methanol molecules from the gas phase without changing the total number of paramagnetic species.

The application of the spectra simulation to determine the relative content of the component paramagnetic species will be illustrated on the example of Mo^{5+} in a poly(acrylic acid) matrix (Mo−PAA),[59] where Mo^{5+} species coordinate oxygen (from carboxylic groups of the matrix) or chlorine ligands (from $MoCl_5$ used for preparing the samples). After activation at 373K two Mo^{5+} species were detected: Mo(A) with $\mathbf{g}_\parallel = 1.967$, $\mathbf{g}_\perp = 1.937$, $\mathbf{A}_\parallel = 81.9$ G, $\mathbf{A}_\perp = 36.7$ G (structural formula I) and Mo(B) with $\mathbf{g}_\parallel = 1.957$, $\mathbf{g}_\perp = 1.934$, $\mathbf{A}_\parallel = 82.0$ G, $\mathbf{A}_\perp \approx 37$ G (structural formula II) (Figure 16a).

I II

The presence of chlorine ligands in the coordination sphere of molybdenum is deduced from the **g** tensor components: $\mathbf{g}_\parallel > \mathbf{g}_\perp$[60] (Table 2, H-1,2). For Mo^{5+} surrounded by oxygen ligands, the reverse relationship occurs: $\mathbf{g}_\parallel < \mathbf{g}_\perp$[40,61] (see also section V.B.1).

Changes in the EPR signals on thermal activation of Mo−PAA samples in the temperature range 473−523 K are shown in Figure 16b,c. At 473 K the EPR signal becomes more symmetrical (Figure 16b) in comparison with Mo(A) and Mo(B) (Figure 16a). The signal detected after heating to 523 K is axially symmetric with reversed **g** values ($\mathbf{g}_\parallel < \mathbf{g}_\perp$) (Figure 16c); this is species Mo(C) with the structural formula III. Simulations indicate the following EPR parameters for Mo(C): $\mathbf{g}_\parallel = 1.902$, $\mathbf{g}_\perp = 1.946$, $\mathbf{A}_\parallel = 94.3$ G, and $\mathbf{A}_\perp = 40.0$ G.

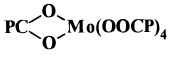

P ≡ polymer
Mo(C)

III

Computer simulations indicate that the EPR spectrum in Figure 16b, for the intermediate activation temperature of 473 K, can be reproduced by assuming a superposition of contributions from Mo(A), Mo(B) and Mo(C) species with relative intensities 2:3:5.

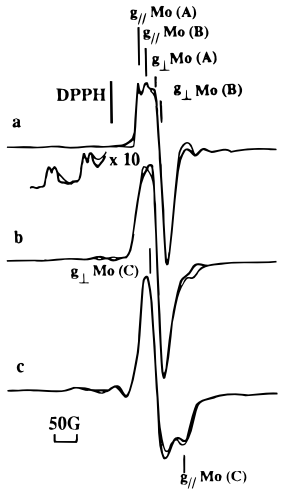

Figure 16. EPR spectra (X-band, 77K) of Mo-PAA (see text) activated in vacuo at 373 K (a), 473 K (b) and 523 K (c). Experimental spectra (thick line), simulated spectra (thin line). (Reprinted from ref 59. Copyright 1993 American Chemical Society.)

V. Correlation between Coordination Chemistry Features and EPR Parameters of Surface TMIs

This review deals mainly with paramagnetic species related to TMIs located on the surface of polycrystalline solids. Suitable supports for metal ions are polycrystalline oxides and zeolites, i.e., crystalline aluminosilicates.

The zeolites are characterized by highly developed and well-defined internal surfaces which make them convenient models for investigating surface phenomena. Various types of natural and synthetic zeolites are known. One of the most frequently used in surface studies is faujasite with the structure presented schematically in Figure 17a.[62] The sites of various symmetry, located in the building units of the faujasite, i.e., supercage, sodalite cages, and hexagonal prisms, are indicated in Figure 17b. TMIs introduced in the zeolite structure by cationic exchange may occupy sites of well-defined symmetry and serve as paramagnetic probes. Depending on their position, they can be accessible for various sized molecules.

EPR spectroscopy can provide a broad spectrum of information concerning such systems, ranging from a simple statement that the sample is paramagnetic and that the paramagnetic species is situated at the surface, to precise assignment of the energy levels involved in the EPR transitions and the distribution of the unpaired spin density on the species. The nature of the central ion, type of bonding with ligands, coordination and symmetry of the surrounding, relaxation mechanism, and the type of motion of the paramagnetic species at the gas (liquid)−solid interface can also be inferred from EPR spectra.

Table 2 schematically outlines the research fields of coordination chemistry and EPR spectroscopy of surface TMIs covered in this review. In this table the correlation between the EPR parameters and coordination chemistry features are indicated by black points. Several examples will be given to show

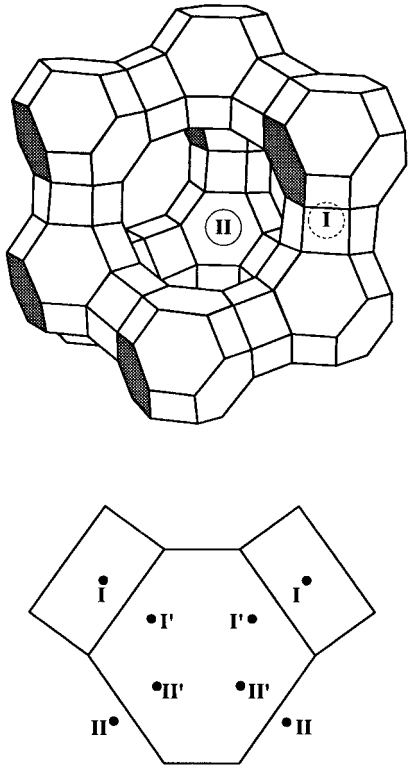

Figure 17. (a) A scheme of the faujasite structure. Aluminum and silicium atoms lie on the corners, oxygen atoms near the edges. Sites I in hexagonal prisms and II in supercage are indicated. (b) A sodalite cage with two hexagonal prisms. Hexacoordinated (I) and tricoordinated (I′, II, II′) cation sites are indicated. (Reprinted from ref 62. Copyright 1968 Elsevier.)

the existence of such correlations and to illustrate the kind of information which may be obtained on surface complexes from EPR spectra.

A. Identification of the Central Ion in a Surface Complex

The assignment of the EPR signal to a particular central ion in a surface complex is usually done on the basis of the **g** tensor values and hf (shf) structure (Table 2). It should be recalled that the interpretation of the spectrum is much easier when the latter feature of the paramagnetic center is available (see also sections III.B, IV.A.2, and V.B.2).

1. Chemical Nature and Oxidation State of the Central Ion

The **g** values of d elements depend on the values of the spin−orbit coupling constant (λ) and crystal field symmetry and strength (Figure 18) (Table 2, D-1,2). High-spin highly symmetric d^5 ions (Mn^{2+}), as well as organic and some non-metal inorganic radicals, show **g** values close to $\mathbf{g}_e$.

With increasing strength of the crystal field, the deviations from the $\mathbf{g}_e$ value decrease for d elements while for f elements, due to the effective screening of the f shell by the external s, p, and d orbitals, the spin−orbit coupling is not disturbed by the crystal field so that **g** values are practically unaffected by the latter. When the separation between the ground state and excited levels is small, the relaxation time is very short, which makes it difficult to observe EPR spectra unless very low temperatures are used (Table 2, D-13).

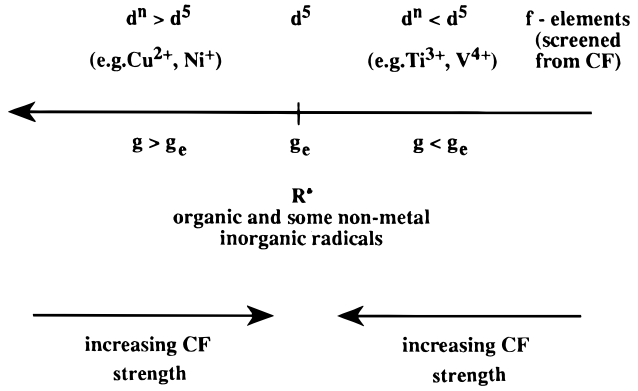

Figure 18. Schematic representation of the relation between **g** values of paramagnetic species and crystal field strength (see text).

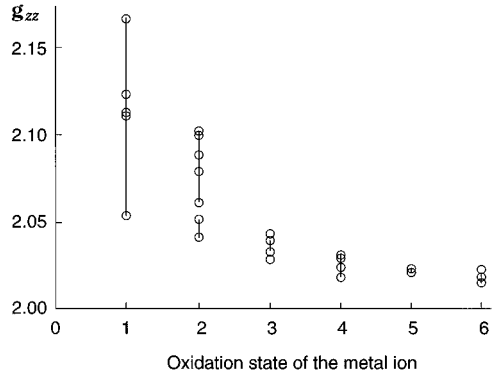

Figure 19. The variation of $\mathbf{g}_{zz}$ of O_2^- ions with the charge of the stabilizing cation. (Reprinted from ref 63. Copyright 1983 Academic Press.)

The non-Kramers ions,[48] with an even number of unpaired electrons (e.g., V^{3+}, Mn^{3+}, Ni^{2+}), are only scarcely observed by EPR, especially in the case of large distortion, because of the large splitting of the energy levels occurring in the absence of the magnetic field under the combined influence of the spin−orbit coupling and crystal field, the so-called *zero field splitting*. In the case when the separation of the levels containing unpaired electron is greater than $h\nu$ they cannot take part in the resonance.

The use of probe molecules, like O_2, may provide information on the oxidation state of the TMI at which the adsorbed species is stabilized, providing e^- transfer can occur. As shown in Figure 19 the $\mathbf{g}_{zz}$ value of the O_2^- radical adsorbed on oxide surfaces is strongly dependent on the positive charge of the nearest cation[63] (Table 2, B-1,14).

Another example may be given by adsorption of NO on copper exchanged, reduced Y zeolites where the EPR features of the created Cu^+−NO species prove the 1+ oxidation state of copper[64,65] (Table 2, B-11,-14). Cu^{2+}Y zeolites exhibit an EPR signal characteristic of Cu^{2+} ions, which strongly decreases upon treatment with CO at 500 °C, indicating reduction of Cu^{2+} into Cu^+ ions. Low-temperature adsorption of NO on CO-reduced samples produces a strong EPR signal (Figure 20) with axial symmetry. Both, in X- and Q-bands, the $\mathbf{g}_\perp$ and $\mathbf{g}_\parallel$ lines exhibit four evenly spaced components, indicating shf interaction of the unpaired electron of the NO radical with the nuclear spin $I = {}^3/_2$ of ^{63,65}Cu isotopes (natural abundance ~100%, Figure 13) (Table 2, A-7,9,10,14). From the shf coupling constant it was calculated, that the

Table 2. Correlation between Coordination Chemistry Features and EPR Parameters (v, value; s, symmetry)[a,e]

		EPR parameters													
				HFS				SHFS							
		g tensor		**A** tensor		number	related	**A** tensor		number	related	integral	line	relaxation	relative to
		v	s	v	s	of lines	intensity	v	s	of lines	intensity	signal intensity	width	time	probe molecules
	coordination chemistry feature	1	2	3	4	5	6	7	8	9	10	11	12	13	14
	Central Atom														
A	nature of paramagnetic ion	•[b]		•		•	•	•		•	•				•
B	oxidation state	•[b]										•			•
C	ground state	•	•											•	•
D	crystal field symmetry and strength	•	•[c]		•[c]				•[c]				•	•	
E	number of paramagnetic ions											•			
	Central Atom−Ligands														
F	coordination number (unsaturation degree)	•	•					•	•	•	•		•[d]	•[d]	•
G	symmetry of the complex (equivalency of ligands, equivalency of atoms in polyatomic ligands)	•	•	•	•	•	•	•	•	•	•		•[d]	•[d]	
H	nature of ligands	•	•	•	•	•	•	•	•	•	•				
I	type of bonding with ligands	•[b]		•				•							
	Transition Metal Ions at Gas (Liquid)−Solid Interface														
K	interaction metal ion−surface	•	•										•		
L	electron transfer	•						•	•	•	•	•			•
M	catalytic reactivity	•	•	•	•	•	•	•	•	•	•				
N	mobility	•	•	•	•								•		

[a] The black points are directly related to the text and/or references listed in footnote *e*. The absence of a point means that there is no correlation or that no example has been found. [b] The **g** tensor values are characteristic of a given transition metal ion in a given surroundings (crystal field symmetry and strength, type of bonding with ligands) and, in this sense, all the examples described in this review may be cited here. [c] It is obvious that the symmetry of the crystal field determines the symmetry of **g** and **A** (HF, SHF) tensors; thus all the examples of EPR spectra with HF and SHF structure described in this review may be cited here. [d] These relations are not discussed in detail in this review but an example based on tetrahedrally and octahedrally coordinated Co(II) differring in relaxation time, i.e., in temperature dependence of the EPR line width can be found in ref 56. [e] References for black points: A-1, section IV.B.; A-3,5,6, 42 and 43; A-7−10, 84; A-7,9,10,14, 64−66, and 89; B-1, 63, 66 and Figure 20; B-11, 64 and 65; B-14, 63−66 and Figure 20; C-1,2, 39, 42, 78, 79, and section V.A.2; C-13, section V.A.2; C-14, 39; D-1,2, Figure 19 and sections V.A.1 and 2; D-12,13, sections V.A.1 and 2; E-11, 40, 53−59, 69, and 70; F-1,2, 39, 40, 70, and 75; F-7−10, 39; F-13, 40; F-14, 39, 40, 58, 69, 70, and 75−77; G-1,2, 39; G-3−6, 63 and 73; G-7−10, 31, 32, and 39; H-1,2, 39, 40, 59, 60, and 69−-71; H-3−6, 27, 31, 32, 63, 73, and 93; H-7−10, 31, 32, and 39; I-3, 93; I-7, 31, 32, 64, 65, and 87; K-1,2, 20, 78, and 79; K-3−6, 20; K-12, 20, 43, 76, 77, 94, and 95; L-1,2, 29; L-7−10, 31, 32, and 85; L-11, 29, 80, 83, and 85; L-14, 80, 82, 83, and 85; M-1,2, 39 and 70; M-3−6, 70; M-7−10, 39, 70, and 87; N-1−4, 20, 78, 79, and 93; N-12, 20, 94, and 95.

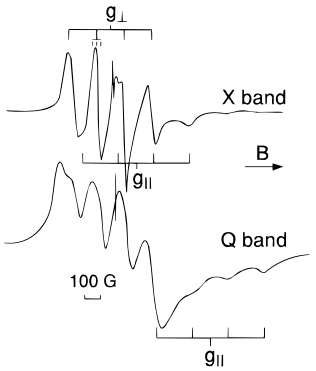

Figure 20. EPR spectra (X- and Q-band, 77 K) of the $Cu^{+}-NO$ complex after adsorption of NO on reduced Cu-exchanged Y zeolite. (Reprinted from ref 65. Copyright 1972 American Chemical Society.)

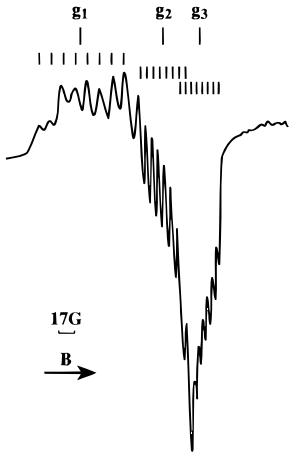

Figure 21. EPR spectrum (Q-band, 77 K) of oxygen adsorbed on V_2O_5/SiO_2. (Reprinted from ref 66. Copyright 1968 Academic Press.)

unpaired electron spends 80% of its time on $2p\pi^*$ orbital of NO and only 20% of its time on Cu^{+}, where it is distributed evenly between the d_{z^2} and 4s orbitals[65] (Table 2, I-7).

The use of a shf structure to identify the adsorption center of oxygen on V_2O_5/SiO_2 is presented in Figure 21.[66] The Q-band spectrum shows that each principal value of the **g** tensor of O_2^- radicals is split into eight components (Table 2, A-7,9,10,14). Such splitting indicates that the unpaired electron of O_2^- ion is coupled with the nuclear spin $I = {}^7/_2$ of the ^{51}V isotope and that the adsorption center is vanadium in its 5+ oxidation state as inferred from the $\mathbf{g}_{zz}$ value of O_2^- (see Figure 19) (Table 2, B-1,14).

Another example is presented in Figure 9, where the hf structure composed of eight lines in both X- and Q-bands indicates interaction of the unpaired electron of d^7 low spin Co^{2+} ions ($S = {}^1/_2$) in a hexacoordinated methyl isocyanide complex with the nuclear spin $I = {}^7/_2$, of the ^{59}Co isotope[42] (Table 2, A-3,5,6).

Both isotopes, ^{51}V and ^{59}Co, have the same nuclear spin ($I = {}^7/_2$), same natural abundance (~100%) (Figure 13), similar theoretical values of the isotropic constant for the free ion,[48] but drastically different hf coupling constants (~80 G for hf of Co and a few gauss for shf of V). For the Co^{2+} ion splitting arises from the interaction of the unpaired electron with its own nucleus (Table 2, A-3), while for O_2^- adsorbed on V_2O_5/SiO_2, the shf pattern is due to the interaction of the unpaired electron of O_2^- with the V^{5+} ion situated on the surface at a distance from the O_2^- radical (Table 2, A-7). The interaction is thus much weaker and the observed splitting consequently much smaller.

2. Ground State of the Central Ion

The ground state of paramagnetic TMIs may be inferred from the dependence of **g** tensor values on crystal field parameters (Table 2).

For d^1 ions in elongated octahedral complexes, the unpaired electron occupies a doubly degenerate ground state (d_{xz}, d_{yz}) and no EPR signal can be observed.[67] In a compressed octahedron, the nondegenerate d_{xy} state lies lowest and for a slight distortion the low lying 2-fold degenerate excited states (d_{xz}, d_{yz}) are close to the ground state (Figure 22a). The small

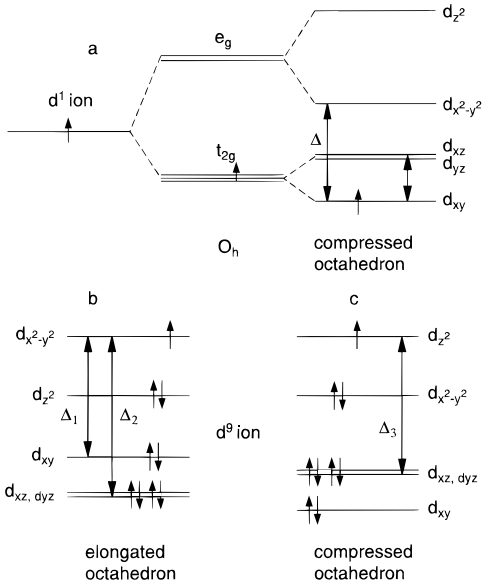

Figure 22. Typical splittings of d orbitals in an octahedral crystal field with tetragonal distortion: (a) compressed octahedron, d^1 ion, (b) elongated octahedron, d^9 ion, (c) compressed octahedron, d^9 ion. This figure only gives the relative ordering of the energy of d orbitals.

energy separation δ results in a short relaxation time and the EPR signal can be observed only at low temperatures (Table 2, D-13). Greater distortions lead to longer relaxation times and EPR signals can be observed at higher temperatures with **g** values:

$$\mathbf{g}_{\parallel} = \mathbf{g}_e - 8\lambda/\Delta \quad \text{and} \quad \mathbf{g}_{\perp} = \mathbf{g}_e - 2\lambda/\delta \qquad (13)$$

where $\Delta = E_{x^2-y^2} - E_{xy}$ and $\delta = E_{xz,yz} - E_{xy}$. Since $\Delta \gg \delta > \lambda$ and, for d^1 ions, $\lambda > 0$, a negative shift in **g** values is observed for these ions (see also section III.A) (Table 2, D-1).

The d^9 configuration corresponds to one electron hole in the d shell, which in ML_6 complexes leads to the so-called Jahn−Teller effect, i.e., spontaneous distortion into a tetragonally distorted octahedron with a $d_{x^2-y^2}$ or d_{z^2} ground state for elongated or compressed octahedron, respectively (Figure 22b,c). In the former case, the **g** values are given by the following equations:

$$\mathbf{g}_{\parallel} = \mathbf{g}_e - 8\lambda/\Delta_1 \quad \text{and} \quad \mathbf{g}_{\perp} = \mathbf{g}_e - 2\lambda/\Delta_2 \qquad (14)$$

where $\Delta_1 = (E_{x^2-y^2} - E_{xy})$ and $\Delta_2 = (E_{x^2-y^2} - E_{xy,yz})$.

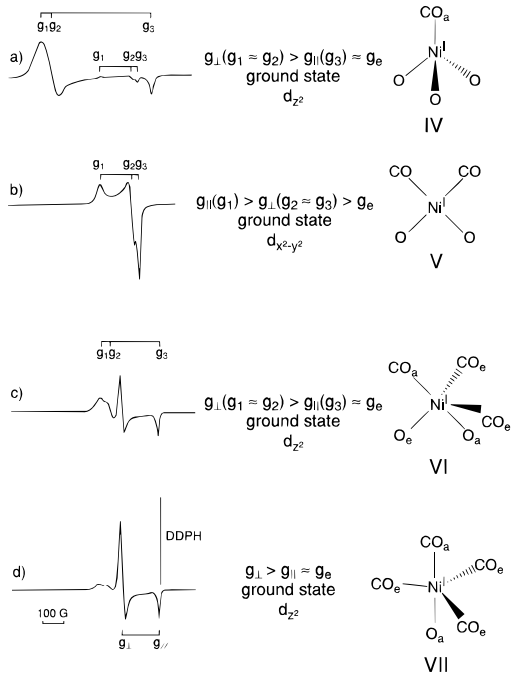

Figure 23. EPR spectra (X-band, 77 K) of Ni^+-carbonyl complexes formed upon CO adsorption on reduced Ni/SiO_2 catalysts under a pressure of (a) 10 Torr CO followed by evacuation at 340 K, (b) 10 Torr, (c) 100 Torr, (d) 400 Torr. For the positions of the ligands, **a** stands for axial and **e** for equatorial (formulae IV, VI, and VII).[39,41]

The spin−orbit coupling constant λ is negative for d^9 ions, and since $\Delta_1 < \Delta_2$, eq 14 leads to the following sequence of **g** values: $\mathbf{g}_\parallel > \mathbf{g}_\perp > \mathbf{g}_e$.

For a compressed octahedron, the **g** components are given by the relations

$$\mathbf{g}_\parallel = \mathbf{g}_e \quad \text{and} \quad \mathbf{g}_\perp = \mathbf{g}_e - 6\lambda/\Delta_3 \qquad (15)$$

where $\Delta_3 = (E_{z^2} - E_{xz,yz})$, which gives the relative order: $\mathbf{g}_\perp > \mathbf{g}_\parallel \sim \mathbf{g}_e$. Such relations were applied to determine the ground state of Ni^+ d^9 ions in a series of carbonyl complexes formed by adsorption of CO on supported Ni^+ ions in Ni/SiO_2, $Ni/SiO_2/Al_2O_3$, and Ni−zeolite systems[39] (see also section IV.A.1) (Table 2, C-1,2,14). Among the four carbonyl species in Figure 23, only the dicarbonyl (species V) shows the relative order: $\mathbf{g}_\parallel(\mathbf{g}_1) > \mathbf{g}_\perp(\mathbf{g}_2 \sim \mathbf{g}_3) > \mathbf{g}_e$ which corresponds to the $d_{x^2-y^2}$ ground state. Thus the degree of electron−ligand interactions taking place in the *xy* plane is larger than that along the *z* axis. This implies symmetries such as elongated octahedron (D_{4h}), square pyramid (C_{4v}), an angular trigonal bipyramid (C_{2v}), trigonal pyramid (C_{3v}), or a square planar arrangement (D_{4h}) (Table 2, G-1,2).

For other species, the relative order $\mathbf{g}_\perp > \mathbf{g}_\parallel \sim \mathbf{g}_e$ indicates a d_{z^2} ground state and stronger interaction of the central Ni^+ ion with the *z* axis ligands of the complex than with those along the *x* and *y* axes. This is the case of a compressed octahedron (D_{4h}) or compressed trigonal bipyramid (D_{3h}). The problem of the symmetry of the Ni^+ carbonyl complexes will be discussed further (see sections V.B.2 and V.C) in relation to the equivalency of CO ligands and shf patterns.

Another example of using **g** tensor values to determine the ground state of the central atom is given by Lunsford and Vansant[42] (Table 2, C-1,2). The relative order: $\mathbf{g}_\perp = 2.087 > \mathbf{g}_\parallel = 2.008 \sim \mathbf{g}_e$ of hexacoordinated low-spin d^7 complex of Co^{2+} in Y zeolite, presented in Figure 9, indicates a d_{z^2} ground state of the complex.

B. Influence of the Ligand Nature on Magnetic Parameters

1. On the g Tensor

The ligands surrounding the central ion doubly bonded to oxygen in a $(M{=}O)L_5^{n-}$ complex may influence the values of its g tensor also via spin−orbit coupling interaction (Table 2). For such a complex of C_{4v} symmetry and with $M = Mo^V$, W^V, V^{IV}, etc., d^1 ions only the $\mathbf{g}_\parallel$ component depends on the spin−orbit coupling constant of ligands, and this dependence is given by the relation:[68]

$$\mathbf{g}_\parallel = \mathbf{g}_e - 2[(2\lambda_M\beta_2\beta_1 - \lambda_L\beta_2'\beta_1')/\Delta E_{(b^2-b^1)}]\,(2\beta_2\beta_1 - 2\beta_1\beta_2'S_{b^2} - 2\beta_2\beta_1'S_{b^1} - \beta_1'\beta_2') \qquad (16)$$

where λ_L and λ_M are the spin−orbit coupling constants of the ligands and of the central metal ion, respectively, β_1, β_2, β_1', β_2' are the linear combination coefficients of atomic orbitals in the expressions of the relevant molecular orbitals and S_{b^1} and S_{b^2} are overlap integrals for the appropriate orbitals. Equation 16 concerns polyatomic species with partially covalent bond while relations 13−15 in the preceding section (V.A.2) were derived on the basis of a simple crystal field approach.

Two examples will be given to illustrate the effect of the ligands on the **g** factor of $(Mo^V{=}O)L_5^{n-}$ surface complexes with (1) different number of oxygen ligands and (2) the same number of ligands but with different electron pair donors.

Reduced, silica-supported molybdenum catalysts prepared by the grafting method[40] exhibit an EPR spectrum (Figure 7) which may be ascribed, as shown in sections IV.A.1 and IV.D, to three different Mo^{5+} species: tetra- (Mo_{4c}^{5+}), penta- (Mo_{5c}^{5+}), and hexacoordinated (Mo_{6c}^{5+}) which all possess a Mo=O molybdenyl bond. Adsorption of polar, oxygen-containing molecules, like water or methanol[40,69,70] caused a stepwise transformation of one molybdenum species into another without changing the total number of Mo^{5+} ions (Figures 15 and 24) (Table 2, E-11, F-14). These results were interpreted in terms of filling the coordination vacancies of Mo^{5+}, according to the scheme presented in Figure 25.

The $\mathbf{g}_\parallel$ value of a molybdenyl species in C_{4v} symmetry depends on the spin−orbit coupling of the ligands surrounding the central atom (eq 16) (Table 2, H-1,2). As the water (or methanol) ligand is connected to the Mo^{5+} ion by the oxygen atom, the spin−orbit coupling constant is the same as that of O^{2-} ion from the SiO_2 support in the Mo/SiO_2 catalyst. Hence the Mo_{4c}^{5+} species, coordinated by one molecule of water (methanol), is expected to give EPR signal similar to that of Mo_{5c}^{5+} while the Mo_{4c}^{5+} species, coordinated by two water (methanol) molecules, is expected to give EPR signal similar to that of Mo_{6c}^{5+}.

The effect of spin−orbit coupling constants of ligands on the **g** tensor of the central atom can be observed in the case of the early steps of preparation

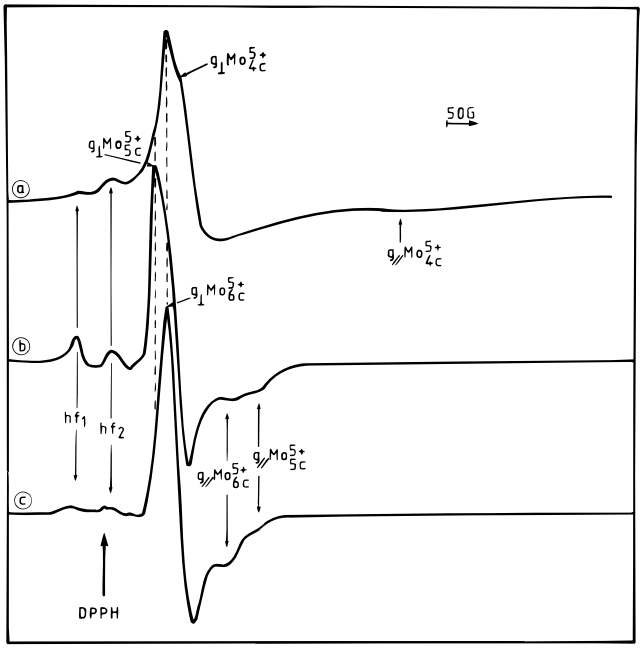

Figure 24. EPR spectra (X-band, 77 K) of oxygen-coordinated Mo^{5+} species formed during thermal reduction of grafted Mo/SiO_2 catalysts (a) and subsequent adsorption of water performed at a pressure of 1 Torr (b) and 18 Torr (c). (From Ref 40. Copyright 1987 American Chemical Society.)

Mo^{5+} species	notation	$g_\perp$	$g_{\|\|}$
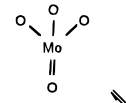	Mo_{4c}^{5+}	1.925	1.750
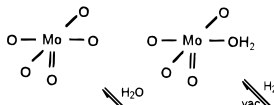	Mo_{5c}^{5+}	1.957	1.866
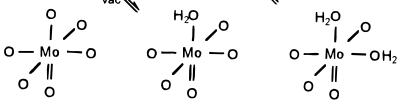	Mo_{6c}^{5+}	1.944	1.892

Figure 25. Schematic presentation of the changes in the coordination sphere of molybdenum species after reduction and water adsorption. Similar scheme applies for methanol or other polar, oxygen-containing molecules (see text and ref 40).

of grafted Mo/SiO_2 catalysts (Figure 26)[71] and for Mo^{5+} complexes in the matrix of polyacrylic acid (Figure 16a)[59] (Table 2, H-1,2). In both cases, molybdenum first introduced as $MoCl_5$ is finally coordinated with O^{2-} and Cl^- ligands. Because of the different spin−orbit coupling constants of oxygen: $\lambda_O = 152\ cm^{-1}$ [72] and chlorine: $\lambda_{Cl} = 587\ cm^{-1}$,[61] which influence the value of $\mathbf{g}_{||}$ (eq 16), the relative orders of the **g** values for $Mo^{V}OL_5^{n-}$ complexes are $\mathbf{g}_\perp > \mathbf{g}_{||}$ for $L = O^{2-}$ (Figures 24 and 16c) and $\mathbf{g}_{||} > \mathbf{g}_\perp$ for $L = Cl^-$ (Figures 26 and 16a).

2. On hf and shf Structures

The nature of the ligands and their position in the coordination sphere of the TMI may be deduced from the shf structure or in the case of paramagnetic ligands from the hf structure of the EPR spectrum (Table 2). Thus, hf patterns have been successfully

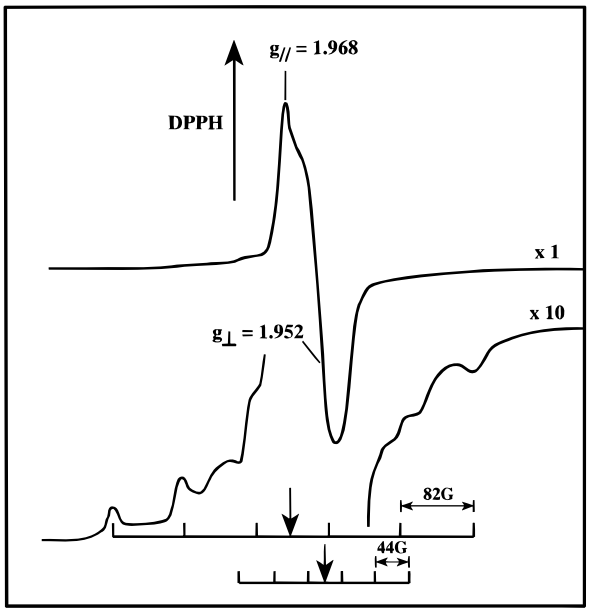

Figure 26. EPR spectrum (X-band, 77 K) of Mo^{5+} coordinated by O^{2-} and Cl^- ions in SiO_2 catalysts grafted with $MoCl_5$. (Reprinted from ref 71. Copyright 1992 Academic Press.)

interpreted leading to the identification of mono- and polynuclear oxygen radical ions adsorbed on metal oxides, i.e., coordinated to surface metal ions[27,63] (Table 2, H-3−6).

The use of the shf structure to show the influence of the ligand on the EPR parameters of a surface complex may be illustrated in the case of the tetracarbonyl complex of Ni^+ in the Ni/SiO_2 system (Figure 6, structure VII in Figure 23)[39] (Table 2, F-7−10,14 G-7−10 H-7−10). The shf splitting arises from the presence of ^{13}C ($I = {}^1/_2$)-enriched CO in the coordination sphere of Ni^+ (see also sections IV.A.1 and V.A.2). The shf pattern consists of 4-fold split doublets centered on each of the axial **g** tensor components. The doublets with the greater coupling constant are related to the axial CO ligand while the quartets are generated by three equivalent CO ligands situated in the equatorial plane of the complex. This leads to the conclusion that the complex adopts a trigonal-bipyramidal structure with only one surface O^{2-} ion. It is interesting to note that the ^{13}C shf constants of the axial CO ligand are roughly twice those of equatorial CO ligands (Figure 6).

The same method applied to the spectra of other carbonyl complexes of Ni^+ leads to the different symmetries indicated in Figure 23: tetrahedral, square planar, and trigonal bipyramid.

C. Symmetry of the Complex—Equivalency of Ligands and Equivalency of Atoms in Polyatomic Ligands

Important information can be derived from the hf splitting of the EPR spectrum on the structural equivalency of ligands coordinated to a central ion and distribution of the unpaired electron density between atoms with $I \neq 0$ in polynuclear ligands (Table 2).

Oxygen enriched in ^{17}O has proved to be a powerful tool to investigate the equivalency of oxygen nuclei

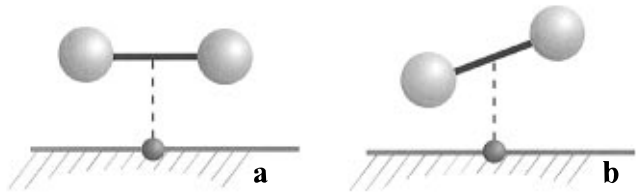

Figure 27. Configuration for equivalent (a) and inequivalent (b) oxygen nuclei, in the O^{2-} surface ion (●, adsorption site). (Adapted from ref 63.)

in O_2^- species adsorbed on oxides[63] (Table 2, G-3−6). For equivalent oxygens (equally distant from the adsorption center) both $^{17}O^{16}O^-$ and $^{16}O^{17}O^-$ give a structure with six lines of equal intensity while $^{17}O^{17}O^-$ leads to a structure of 11 lines with intensities varying from 1 to 6 due to degeneracy in the levels.

In the case of O_2^- adsorbed on silica-supported molybdenum[73] the oxygen nuclei are inequivalent, then $^{17}O^{16}O^-$ and $^{16}O^{17}O^-$ become distinct species with two different six-line structures and a single ^{17}O nucleus ($^{17}O^{16}O^-$ and $^{16}O^{17}O^-$ species) and a 36-line structure for the $^{17}O^{17}O^-$ species with two ^{17}O nuclei (Table 2, G-3-6 H-3-6).

The observed inequivalency of oxygens in O_2^- ion adsorbed on supported molybdenum[73] indicates their different distance to the adsorption center. This occurs when the O_2^- ion has some covalent bonding to the surface cation and assumes an angle to the surface. This configuration is called bent or "end-on" in opposite to the parallel or "side-on" arrangement (Figure 27).

The O_2^- superoxide species consistent with either "side-on" and equivalent oxygens or covalent "end-on" configuration and inequivalent oxygens are formed on CoO−MgO solid solutions[31,32] (see section V.E.1).

The previous examples illustrate the use of hf parameters to study the equivalency of atoms within a polyatomic ligand. The problem of equivalency of ligands has also another aspect, related to various positions occupied by the ligands in the coordination sphere of the central ion and to the symmetry of the whole complex. An example of using shf structure to determine this type of equivalency in Ni^+ carbonyl complexes was presented in section V.B.2 (Table 2, G-7-10).

D. Chemical Bonding between the Central Ion and the Ligands

The EPR spectrum of a surface TMI may contain information on the nature of its bonding with the surrounding ligands, providing the central metal ion or atoms coordinated as ligands contain isotopes with nuclear spin $I \neq 0$ (Table 2). The hf coupling constant depends on the spin density distribution over the nuclei "seen" by the unpaired electron. Separation of the hf (shf) tensor into its isotropic and anisotropic components provides information on the nature of the orbitals hosting the unpaired electron. The isotropic component is related to the unpaired spin density on orbitals with s-character while the anisotropic component is related to the electron occupancy of the p, d or other directional orbitals. From the values of spin density on particular atoms, the character of their bonding (ionic or covalent) to the central ion can be derived.

The superoxide species consistent with either an ionic model, i.e., electrostatic interaction with surface cation, or with partially covalent metal−ligand bond are formed on the surface of CoO−MgO solid solutions[31,32] (Table 2, I-7).

E. Reactivity of Surface Transition Metal Ions

Surface ions possess lower coordination numbers than those situated in the bulk (Figure 2). The reason of this unsaturation is that at the crystal faces, corners, or edges there are fewer rigid lattice neighbors and that volatile ligands like H_2O and CO, coordinated by surface TMIs, may be easily removed, e.g., by vacuum or thermal treatment leaving vacancies in their coordination sphere. Interaction with gas-phase molecules completes the coordination sphere of surface metal ions. In the case of strong interaction reactions within the inner sphere of the surface complex may occur.

Interactions caused by unsaturation of surface metal ions occur also at the solid−liquid interfaces. Oxide catalysts are often obtained by hydrothermal processes consisting in deposition (grafting, impregnation) of TMIs onto oxide support from water or organic solvent solutions. EPR studies of different steps of catalyst preparation and catalytic reactions were recently reviewed by Che and co-workers.[74] Different kinds of interaction, of physical or chemical nature, occur at the liquid−solid interface which may change the mobility of transition metal complexes in solution or provoke significant modification of their coordination sphere, e.g., by exchange of ligands with O^{2-} oxide ions from the surface.

Examples illustrating how the features related to unsaturation of the surface TMIs may be revealed at gas (liquid)−solid interfaces by using probe molecules (Table 2) are given below (see also sections IV.A.2, IV.D, and V.B.1).

1. Ligand Addition and/or Substitution

a. Gas−Solid Interface. *i. Without Changing the Number of Bonds of the TMI with the Surface.* The unsaturation degree of surface ions can be determined from the number of small probe molecules entering their coordination sphere and increasing the coordination number provided the total number of spins does not change, i.e., that no redox (e^- transfer) reaction takes place (Table 2). The illustration of such behavior is given in sections IV.D and V.B.1 on example of tetra- (Mo_{4c}^{5+}) and penta-coordinated (Mo_{5c}^{5+}) species in silica-supported reduced molybdenum catalyst adsorbing gas-phase molecules.[70,75] In this case, the probe molecules complete only the coordination sphere of coordinatively unsaturated TMIs without changing the number of bonds with the surface (Table 2, F-1,2,14).

ii. Changing the Number of Bonds of the TMI with the Surface. The interaction of surface TMIs with gas-phase molecules may also lead to reversible changes in the number of bonds with the surface occurring when the ligand pressure in the gas phase is varied. This effect was observed on silica-supported Ni^+ ions[39] (see also sections IV.A.1 and V.B.2) (Table 2, F-1,2,7-10,14, G-1,2,7-10, H-1,2,7-10). Four different types of complexes were observed (Figure 23), and it was concluded that, depending on the CO

pressure, one to four CO molecules can enter the coordination sphere of the Ni^+ ion while the number of surface oxygens acting as ligands decreases from three to one.

The same method was applied to other Ni^+-containing supported catalysts.[76,77] The common feature to all these systems is the strong dependence of the type of carbonyl complex on the CO pressure, reversibility of the reaction with CO, and EPR parameters characteristic for the species of a given symmetry (Figure 23).

The main difference consists in the line width which increases in the following sequence: $Ni/SiO_2 < NiCa-X < Ni/Al_2O_3 \approx Ni/TiO_2 \approx Ni-TiO_2/SiO_2$.

The broadening effect may be attributed for one part to the unresolved shf splitting due to the interaction of the unpaired electron of Ni^+ with ^{23}Al nucleus ($I = {}^3/_2$, abundance 100%), ^{47}Ti ($I = {}^5/_2$, abundance ~8%), and ^{49}Ti ($I = {}^7/_2$, abundance ~5%) nuclei (Figure 13). This may be an indication of the existence of Ni−O−Al[76] and Ni−O−Ti[77] bonds (Table 2, K-12). The broadening can result also from inequivalent surface sites leading to a range of different **g** tensor components and an increased line width.

b. Liquid−Solid Interface. In certain cases, interactions between the solid surface and TMIs in aqueous solution are strong enough to modify the coordination sphere of aqua complexes. This occurs, e.g., in the case of Cu^{2+} ions in Y zeolites.[78,79] EPR measurements were performed on copper-exchanged Y zeolites containing less than five Cu^{2+} ions per unit cell to avoid dipolar broadening. At room temperature, fully hydrated CuY zeolites give a broad, almost symmetric EPR line with $\mathbf{g}_{av} = 2.19$. At 77 K, a typical spectrum of polycrystalline paramagnetic species of axial symmetry was observed with a hf splitting, indicating interaction of the unpaired electron with $^{63,65}Cu$ nuclei [$I = {}^3/_2$, abundance ~100% (Figure 13)] and with $\mathbf{g}_{\|} = 2.38-2.33$ and $\mathbf{g}_{\perp} = 2.07$ (i.e., $\mathbf{g}_{\|} > \mathbf{g}_{\perp} > \mathbf{g}_e$), indicating that the unpaired electron is in a $d_{x^2-y^2}$ orbital (section V.A.2 and Figure 22b) (Table 2, C-1,2). This finding implies that in fully hydrated zeolites Cu^{2+} ions are present as hexaaqua complexes $[Cu(H_2O)_6]^{2+}$ and that the crystal field at the cupric ion has a tetragonal symmetry due to the Jahn−Teller effect. At room temperature, the complex is free to tumble rapidly which averages out the anisotropic terms and hence results in a symmetric EPR line (Table 2, N-1-4). This is an indication, that the $[Cu(H_2O)_6]^{2+}$ complex does not interact strongly with the zeolite surface (Table 2, K-1,2). At 77 K the complex is frozen and tumbling is precluded, leading to the anisotropic spectrum. These changes are reversible upon changing the recording temperature.

Upon dehydration, anisotropic EPR spectra were observed at room temperature with an irreversible change in the **g** values upon recording temperature. It was concluded, that after removing water molecules from the coordination sphere of copper, the Cu^{2+} ions migrate toward the walls of the zeolite and coordinate with lattice O^{2-} ions (Table 2, K-1,2 N-1-4). The EPR parameters point out that fully dehydrated Cu^{2+} ions occupy S_I and $S_{I'}$ sites in the zeolite structure (Figure 17). In this case the zeolite structure, entering the coordination sphere of Cu^{2+} via its surface O^{2-} ions, acts as a supramolecular polydentate ligand.[9]

Interaction of Cu^{2+} ions with the structure of clay minerals, saponites, pillared with polyhydroxo complexes of aluminum, was shown by EPR[20] (Table 2, K-1-6). Fixation of Cu^{2+} at the pillars leads to the broadening of EPR signals due to the unresolved shf interaction of unpaired electron of Cu^{2+} with the nuclear spin of ^{27}Al ($I = {}^5/_2$, abundance 100%[48]) (Table 2, K-12).

2. Electron-Transfer Reactions

Redox properties of TMIs on solid surfaces can be studied at the gas−solid or liquid−solid interfaces by using electron acceptor/donor probe molecules (Table 2). Charge transfer reactions occur between the solid surface and the probe molecule:

$$S + A \rightarrow S^+ + A^- \quad (17)$$

$$S + D \rightarrow S^- + D^+ \quad (18)$$

where S denotes a surface ion, while A and D represent an electron acceptor or donor molecule, respectively. The probe molecules can react from the gas phase or from solutions involving organic solvents.

Different kinds of information can be obtained from this type of studies. For instance, the threshold value of electron affinity (EA) of the acceptor molecule (A) or ionization potential (IP) of the donor molecule (D) at which the charge transfer starts to be observed, characterizes the reducing or oxidizing strength of the surface sites, respectively. The number of redox centers is given by the intensity of the EPR signal of radicals formed by electron transfer from the surface donor sites to the adsorbed (A) molecule or from the adsorbed (D) molecule to the surface electron acceptor centers. The hf (shf) structure of the EPR spectrum of adsorbed A^- or D^+ radical ions gives information about the surface site at which the adsorbed species is localized. Very often, the stabilizing site of the adsorbed A^- or D^+ radical ion is different from the donor/acceptor site. In some cases, EPR studies can even provide information on the mechanism of electron transfer on oxide surfaces.

We will use CoO−MgO solid solutions and silica or alumina-supported MoO_3 as model systems to illustrate the whole range of information which can be obtained using EPR.

The electron donor properties of the CoO−MgO solid solutions with CoO content 0−15.3 mol % were investigated using adsorption of nitrobenzene (NB, EA = 1.05 eV), *m*-dinitrobenzene (DNB, EA = 1.75 eV), tetracyanoethylene (TCNE, EA = 2.5 eV), and perylene (PE, EA = 0.71 eV) dissolved in benzene[80] (Table 2, L-14). On pure MgO as well as on CoO−MgO solid solutions pretreated in vacuo at 500 °C, NB, DNB, and TCNE gave rise to EPR signals of the corresponding anion radicals A^- produced by reaction 17, while PE reacted only with CoO−MgO solid solutions. The EPR features of the radical formed upon PE adsorption as well as its reactivity toward molecular oxygen to form O_2^- suggest that it can be identified as the anion radical (PE^-). The fact, that PE^- can be formed exclusively in the presence of Co^{2+} ions indicates that the latter are the strongest

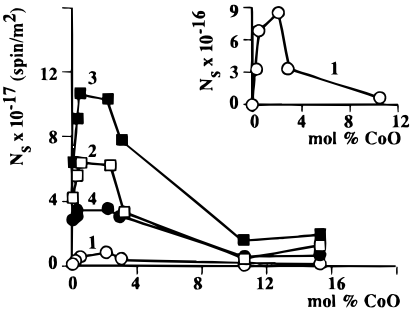

Figure 28. EPR signal intensity of radical ions A^- produced from perylene (PE) (1), nitrobenzene (NB) (2), *m*-dinitrobenzene (*m*-DNB) (3), and tetracyanoethylene (TCNE) (4) on CoO−MgO solid solutions as a function of CoO concentration. The curve (1) has been enlarged and presented in the upper part of the figure. (Reprinted from ref 80. Copyright 1985 Elsevier.)

electron donors in the CoO−MgO system. The dependence of the EPR signal intensity of the radical ions A^- vs CoO concentration is similar for all the electron acceptors (Figure 28) (Table 2, L-11).

As shown by theoretical calculations,[81] only the most coordinatively unsaturated O_{3c}^{2-} ions lose enough of their lattice energy to become effective donors for commonly used electron acceptors: $O_{3c}^{2-} + A \rightarrow O_{3c}^{-} + A^-$. The O_{3c}^- ions further react with an excess of acceptor A:[82] $O_{3c}^- + A \rightarrow {}^1/_2O_2 + A^-$. The amount of O_{3c}^{2-} ions is closely related to the presence of steps, corners, and high index planes formed during thermal activation of the solid solutions in vacuo.[83] The small concentration of electron donor centers in the concentration range 10.4−15.3 mol % CoO (Figure 28) may be related to the decrease of specific surface area,[80] which erodes the surface steps and favors the formation of low index planes (Table 2, L-11,14).

Dilute CoO−MgO solid solution with low content of CoO (∼3 mol %) contain mainly isolated Co^{2+} ions. Those ions have been found recently to function as heterogeneous oxygen carriers, i.e., they are able to reversibly adsorb oxygen according to the process:[31,32] $Co^{2+} + O_2 \leftrightarrow Co^{3+} + O_2^-$. By adsorption of oxygen at 77 K below 0.1 Torr, a complex spectrum with distinct shf structure arising from ^{59}Co [$I = {}^7/_2$, natural abundance ∼100% (Figure 13)] is obtained (Figure 29a) showing two slightly different O_2^- "end-on" centers (species I and II in Table 3) stabilized on Co^{3+} ions (Table 2, G-7-10, H-7-10, L-7-10). The spectrum in Figure 29a corresponds to the initial stage of the oxygen interaction with the CoO−MgO system, since the two species, stable at 77 K, undergo different evolution upon evacuation accompanied by a slow rise of temperature to about 120−150 K. This treatment leads to the spectrum of Figure 29b (recorded at 77 K) composed of two superimposed signals. The first one belongs to a new species with Co shf structure and orthorhombic **g** and **A** tensors (species III in Table 3). By comparison with parallel IR data,[31,32] species III has been assigned to a

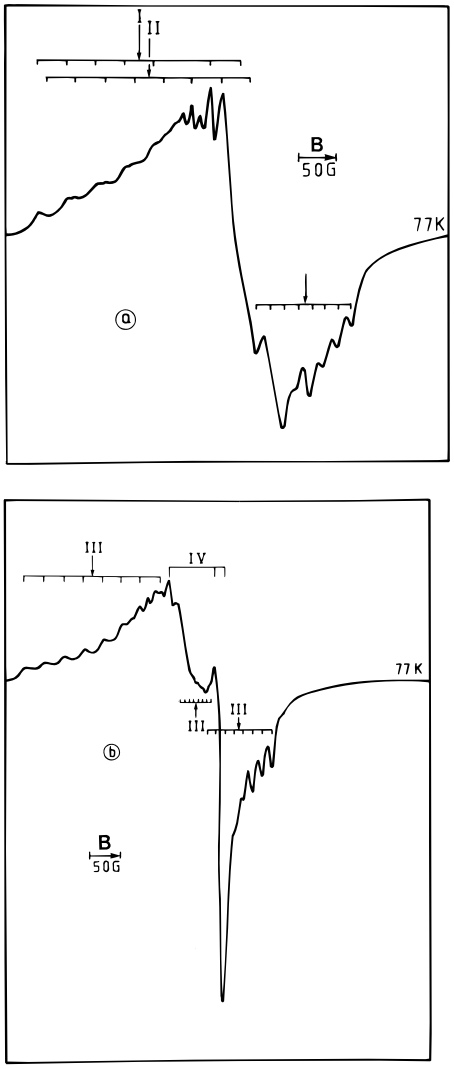

Figure 29. EPR spectra (X-band, 77K) of $^{16}O_2^-$ adsorbed on CoO−MgO: (a) species I and II (Table 3) obtained after oxygen adsorption at 77 K and removing excess of oxygen; (b) species III and IV (Table 3) obtained after slow heating of the adsorbed species I and II to about 120−150 K and pumping. (Reprinted from ref 31. Copyright 1986 American Chemical Society.)

superoxide ion O_2^-, adsorbed on a Co^{3+} center and further stabilized by interaction with a neighboring Mg^{2+} ion. The second signal (species IV in Table 3) is due to O_2^- adsorbed on Mg^{2+} ions.

The features of species III disappear upon evacuation at room temperature but can be restored by oxygen readmission at the same temperature. If oxygen is readsorbed at 77 K, species I and II are formed instead of species III. Species IV, which is the most stable, is destroyed only above 500 K. The molecular nature of these various species has been confirmed with ^{17}O-enriched oxygen.[32] The analysis of the hf structures due to the nuclear spin $I = {}^5/_2$ of the ^{17}O isotope leads one to conclude that species I, II, and III have inequivalent oxygen nuclei corre-

Table 3. Spin Hamiltonian Parameters of Oxygen Species on CoO−MgO Surface (from ref 31)

species	$\mathbf{g}_1$	$\mathbf{g}_2$	$\mathbf{g}_3$	$\mathbf{A}_1$[G]	$\mathbf{A}_2$ (G)	$\mathbf{A}_3$ (G)
I: O_2^-/Co^{3+}	2.120	ill-defined	1.983	38	ill-defined	17.5
II: O_2^-/Co^{3+}	2.113	ill-defined	1.983	38	ill-defined	17.5
III: $O_2^-/Co^{3+},Mg^{2+}$	2.141	2.033	1.990	31	7	15.0
IV: O_2^-/Mg^{2+}	2.077	2.009	2.002			

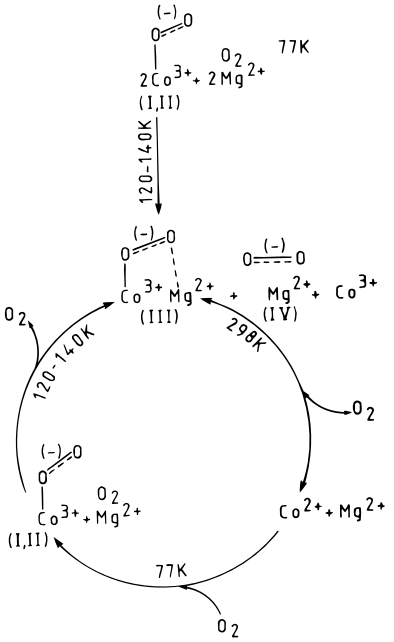

Figure 30. Scheme of the interaction of oxygen with the CoO−MgO solid solutions. (Reprinted from ref 31. Copyright 1986 American Chemical Society.)

sponding to a bent $Co^{3+}O_2^-$ structure while species IV assigned to $Mg^{2+}O_2^-$, exhibits equivalent oxygen nuclei equidistant from the Mg^{2+} surface cation (Table 2, H-3−6). The results have been summarized in Figure 30, where the cycle indicates the reversible nature of oxygen adsorption.

In addition to the monomeric Co adducts described above, Howe and Lunsford[84] have also described mono- (O_2:Co = 1:1) and dimeric (O_2:Co = 1:2) species in CoY zeolite. A dimeric peroxodicobalt adduct $[Co^{3+}L_xO_2^{2-}Co^{3+}L_x]^{4+}$, where L = NH_3 or CH_3NH_2, can be oxidized to give a superoxodicobalt species $[Co^{3+}L_xO_2^-Co^{3+}L_x]^{5+}$, which is paramagnetic and gives a characteristic set of 15 lines in the EPR spectrum due to shf interaction with two equivalent ^{59}Co nuclei (Figure 31) (Table 2, A-7-10).

The formation of superoxide O_2^- ions on oxide surfaces may also occur with electron transfer from the bulk of the oxide, as shown for oxygen adsorbed on reduced ^{95}Mo-enriched MoO_3/Al_2O_3.[85] The presence of O_2^- radicals interacting with the nuclear spin of Mo ($I = 5/2$) was observed after oxygen adsorption at 77 K, while on warming to 300 K a shf structure, characteristic of oxygen adsorbed on Al^{3+} (^{27}Al, $I = 5/2$, abundance 100%[48]), appeared. The total concentration of O_2^- ions increased on warming, and O_2^- stabilized on Mo^{6+} can still be observed if the sample was cooled to 77 K. Thus, formation of O_2^- stabilized on Al^{3+} was related to electron transfer not from O_2^- stabilized on Mo^{6+} but from reduced molybdenum sites, not available at 77 K. The electron transfer can then be envisaged from Mo_b^{5+} ions located in the bulk (Figure 32). These results are in line with EPR measurements[26] which show that molybdenum ions deposited on the support surface can migrate at moderate temperatures into the bulk of the matrix where they are stabilized as Mo^{5+} ions and then serve as a reservoir of electrons (Table 2, L-7-11).

Electron transfer on oxide surfaces may occur, as in coordination compounds, via inner- or outer-sphere mechanism. The inner-sphere electron-transfer mech-

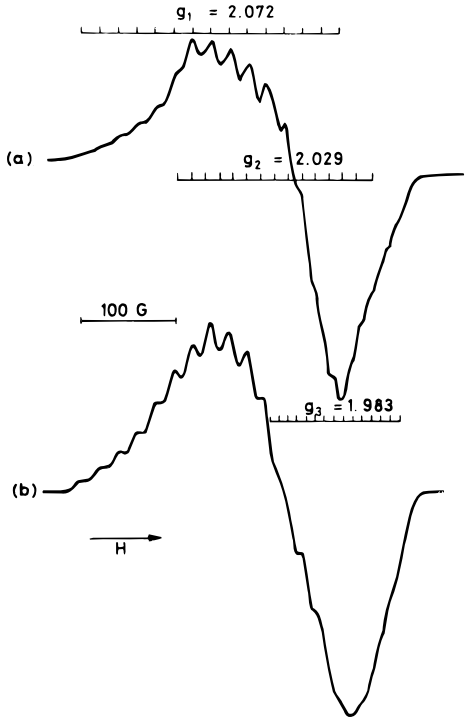

Figure 31. EPR spectra of $[Co^{3+}(NH_3)_xO_2^-Co^{3+}(NH_3)_x]^{5+}$ in CoY zeolite: (a) experimental spectrum (X-band, 77 K), (b) simulated spectrum. (Reprinted from ref 84. Copyright 1975 American Chemical Society.)

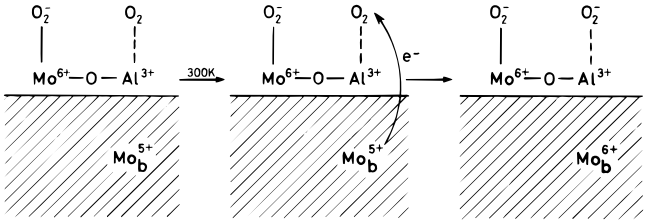

Figure 32. Electron transfer occurring at the surface of MoO_3/Al_2O_3 from Mo_b^{5+} ions located in the bulk. (Reprinted from ref 63. Copyright 1983 Academic Press.)

anism operates, e.g., in the process of formation of O^- radicals occurring by thermal decomposition of N_2O adsorbed on reduced Mo/SiO_2 catalysts[29] (for characterization of the Mo/SiO_2 catalyst see sections IV.A.1, IV.D, and V.B.1). The adsorption occurs only on coordinatively unsaturated tetracoordinated Mo_{4c}^{5+} species which is transformed to pentacoordinated Mo_{5c}^{5+} (Table 2, L-1,2):

$$Mo_{4c}^{5+} + N_2O \rightarrow [Mo_{4c}^{5+}-N_2O] \qquad (19)$$

The electron transfer then occurs from Mo^{5+} to N_2O ligand via an inner-sphere mechanism. This step is followed by thermal decomposition of the N_2O^- species with formation of the O^- radical:

$$[Mo_{4c}^{5+} - N_2O] \rightarrow [Mo_{4c}^{6+}-N_2O^-]^* \rightarrow [Mo_{4c}^{6+}-O^-] + N_2 \qquad (20)$$

The intermediate species $[Mo_{4c}^{6+}-N_2O^-]^*$ is not detected by EPR, due to a lifetime that is too short.

At temperatures above 150 °C, another reaction, occurring via an outer-sphere mechanism, competes with reaction 20. It consists in the electron transfer

from external Mo_{5c}^{5+} and Mo_{6c}^{5+} ions surrounding the $[Mo_{4c}^{5+}-O^-]$ species to the O^- ligand:

$$Mo_{5c,6c}^{5+} + [Mo_{4c}^{6+}-O^-] \rightarrow Mo_{5c,6c}^{6+} + [Mo_{4c}^{6+}-O^{2-}] \quad (21)$$

This process can be followed by the decrease of the intensity of both Mo^{5+} and O^- EPR signals (Table 2, L-11).

3. Catalytic Reactions within the Inner Sphere

Two examples will be given to illustrate the coordination chemistry approach to the EPR studies of the mechanism of catalytic reactions (Table 2): dimerization of olefins and oxidation of methanol, both occurring on the surface of oxide catalysts.

a. Dimerization of Olefins. As Ni^+ ions are the active sites in the homogeneous olefin dimerization reaction,[86] the coordination of ethene onto supported Ni^+ ions has also been investigated[39] (Table 2, M-1,2,7-10). The dicarbonyl species (V in Figure 23) progressively reacts with ethene, giving rise to a complex spectrum assigned, by employing ^{13}C-enriched CO, to the $[Ni(CO)_2(C_2H_4)]^+$ species (VIII), with two inequivalent CO ligands. The similarity between the EPR **g** tensors of the tricarbonyl complex of Ni^+ (VI in Figure 23) and species VIII suggests that the structure of the latter is probably a trigonal bipyramid with one axial CO_a ligand and one equatorial CO_e ligand associated with a large and about twice smaller hf coupling constants, respectively.

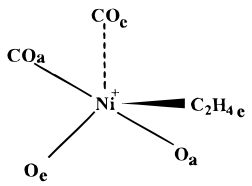

VIII

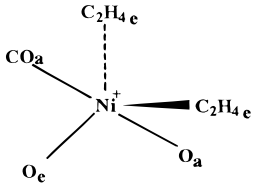

IX

Thus the ethene molecule is in an equatorial position and species VIII is obtained by addition of one ethene molecule to species V (Figure 23). Increasing the ethene pressure up to 600 Torr caused a further change in the EPR spectrum. By using ^{13}C-enriched CO, a new species, IX, can be identified again with a trigonal-bipyramid structure and the CO molecule in axial position while the two ethene molecules are in equatorial positions. The species IX, $[Ni(CO)(C_2H_4)_2]^+$, is obtained from species VIII by ligand exchange, i.e. by replacing CO_e in the complex by $(C_2H_4)_e$.

Catalytic activity tests were performed on systems containing the two species VIII and IX. With species VIII, no appreciable olefin dimerization is observed to take place after 24 h, whereas with species IX, olefin dimerization does occur. The product distribution is very close to that observed in the catalytic tests performed without carbon monoxide. It seems therefore necessary that two ethene molecules should be bonded to the same Ni^+ ion for dimerization to take place. It is important to note that there are four types of ligands around the Ni^+ ion: (1) the reactants which are transformed into the products (i.e., the second type of ligands), (3) the CO spectator ligand, which all are *mobile* ligands, and finally (4) the *rigid* surface O ligand.

When alkylphosphines rather than CO are used as spectator ligands, two effects are observed.[87] The first, of electronic nature, is proportional to the number and basicity of the alkylphosphines introduced and leads to an increase on the electronic density at the metal center (Table 2, I-7, M-7-10). The consequence is a weakening of the affinity for soft Lewis bases such as the reaction products (for instance, butenes for ethene dimerization) and an increased stability of the catalyst by a weakening of the chemical bond between Ni^+ and the products. In addition to this electronic effect, a conjugated steric effect due to both the surface and the spectator ligand is superimposed.[88] For instance, with bulky alkylphosphines, the selectivity can be drastically increased in 1-butene[87] or 2,3-dimethyl-1-butene[89] for ethene and propene dimerization, respectively.

b. Oxidation of Methanol. Methanol oxidation, via the selectivity of the products obtained, appears to be one of the most suitable probes of catalytic surfaces. Known to be structure sensitive,[90,91] this reaction can also distinguish acid−base from redox catalytic sites.[92] In addition, it was found to be very sensitive to molybdenum dispersion, by comparing silica-supported molybdenum catalysts prepared by impregnation and grafting, with low and high dispersion respectively.[75] On the former catalysts, formaldehyde is the main product. On the latter ones, the relative amounts of formaldehyde and methyl formate, which are the main products, depend on molybdenum dispersion, the latter product becoming more important for increasing dispersions.

The mechanism of methanol oxidation[70] (Table 2, E-11, M-1-10) which involves elimination of two different hydrogens coming from the methyl (nonacidic H) and hydroxyl (acidic H) groups consists of two consecutive reactions. In the first, the methyl hydrogen is extracted homolytically by the O^- ligand in the LLHT (ligand-to-ligand hydrogen transfer) elementary process and the reductant intermediate $^{\bullet}CH_2OH$ is formed. The second, more complex step, involves reduction of Mo^{6+} via LMET (ligand-to-metal electron transfer) accompanied by a proton release from the OH group due to the acid−base type interaction with O^{2-} ligand (LLPT, ligand-to-ligand proton transfer). This mechanism is consistent with the variation of selectivity in methyl formate and aldehyde with Mo dispersion. Indeed, on highly dispersed Mo catalyst such as grafted Mo/SiO_2, the decay of $^{\bullet}CH_2OH$ by redox process involves their migration onto the silica support. This makes possible the side reactions with carrier surface groups such as $SiOCH_3$, opening pathways for methyl formate formation. On the other hand, for bulk MoO_3 or low dispersed Mo on MoO_3/SiO_2 catalyst prepared by impregnation, where the Mo adsorption sites are in close interaction and involve at least pairs of reducible Mo^{6+} ions, the two processes LLHT and LMET-LLPT are spatially coupled, i.e., take place at the same active entities. No migration of intermediate radicals is required and CH_2O becomes the main product of methanol oxidation. The study provided evidence that the reaction takes place within the

coordination sphere of molybdenum, revealing directly the role of coordinatively unsaturated Mo^{6+}/Mo^{5+} ions redox couples as the reaction active centers.

F. Mobility at the Gas (Liquid)–Solid Interface

Changes in the environment of molecules adsorbed at the gas-solid or liquid-solid interface, caused by their motion occurring at various temperatures, play an important role in determining the reactivity of the molecules. The relevant theory was developed by Freed.[93] The temperature dependence of EPR spectra can be used to conclude about the mechanism of motional dynamics.

1. Gas–Solid Interface

Temperature-dependent EPR spectra of O_2^- adsorbed on Ti ions supported on porous Vycor glass were analyzed by Freed and co-workers[94] in the temperature range 4.2−400 K. It was shown that the position of the **g** tensor component perpendicular to the internuclear axis of O_2^- remained constant in the investigated range of temperatures, whereas two other components shift in position which was accompanied by drastic line-shape changes. These results indicate that the molecular motion of O_2^- on the surface is highly anisotropic, consisting essentially of the rotation about the axis perpendicular to the internuclear axis of O_2^-. The analysis of ^{17}O hf structure of O_2^- suggested that the internuclear axis is tilted slightly from the surface, i.e. that one oxygen is closer to the Ti^{4+} (Figure 27b). Simulation of the EPR spectra showed that different mechanisms of motional dynamics are operating at various temperatures. The interpretation of the EPR results was confirmed by extended Hückel calculations performed by Freed and co-workers.[95]

Another example of motion of the O_2^- radical on oxide surfaces is given by Howe and co-workers.[96] An O_2^- species adsorbed on silica-supported tungsten was identified with a temperature-dependent shape of the EPR signal, indicating anisotropic motion on the surface. The spectrum observed at 77 K was assigned to an O_2^- radical with equivalent oxygen atoms. The hf structure observed with ^{17}O-enriched oxygen can be fitted to an axially symmetric hf tensor with the unpaired electron completely localized on the dioxygen (Table 2, H-3-6, I-3). The invariance of $\mathbf{A}_{yy}$ with increasing temperature indicates that the motion of the adsorbed radical is occurring predominantly around the *y* axis (Table 2, N-3-4).

The reorientation of the O_2^- surface species adsorbed on the γ-Al_2O_3-supported [Co^{II}(ph)] (ph = phthalocyaninato) was investigated by Barzaghi and co-workers.[97] The unusual symmetry of the EPR signal of Co(II) adduct and its change with temperature indicated the occurrence of a motion of O_2^- from one [Co^{II}(ph)]−γ-Al_2O_3 site to another. The authors discuss the possible relevance of this behavior to catalytic purposes.

The temperature-dependence of EPR spectra provides information not only on the mobility of paramagnetic species adsorbed on oxide surfaces but also on their stabilization at various surface centers. This aspect is illustrated in section V.E.2 on an example of O_2^- radical produced on the surface of CoO−MgO solid solutions[31,32] by electron transfer from a Co^{2+} donor center to O_2 molecule. The radical can be then stabilized on Co^{3+} or Mg^{2+} surface ions, depending on temperature.[31]

2. Liquid–Solid Interface

In water solutions, TMIs coordinate water molecules, forming aqua complexes which are usually free to rotate and migrate within the liquid medium. The mobility of the complex is, however, strongly modified in the vicinity of the surface and inside the pores.[98] Distinct effects of temperature and of pore diameter on the mobility of Cu^{2+} complexes in a set of copper impregnated silicas were found by Bassetti and co-workers[99] (Table 2, K-12, N-12).

Comparison of EPR spectra of wet and dry samples of saponites pillared with polyhydroxo complexes of aluminum and containing adsorbed Cu^{2+} ions allows easy discrimination between mobile and immobile Cu^{2+} species[20] (Table 2, N-1-4,12).

VI. Time-Resolved EPR To Study the Location and Mobility of TMIs in Various Systems

Time-resolved EPR spectroscopy is becoming increasingly useful in studying the surroundings of paramagnetic TMIs on a variety of oxide and aluminosilicate (phosphate) surfaces. Electron spin echo envelope modulation (ESEEM) spectra show a periodic modulation of the echo amplitude which arises from hf interactions with nearby nuclear spins. Analysis of the ESEEM spectra allows determination of hf coupling constants which are too small to be measured in conventional EPR spectra. Thus information on the identity, number, and distance of weakly interacting nuclei may be obtained.

The ESEEM method was successfully applied to study the location and coordination of TMIs in mesoporous and microporous materials which are of considerable importance as molecular sieves and selective catalysts.

Mesoporous materials (MP) with pore diameters in the range 20−500 Å are typically amorphous or paracrystalline solids such as silicas,[100] aluminas,[101] or modified layered materials such as pillared clays and silicates.[102−104] The synthesis of these materials involves the use of ionic surfactants which interact with the inorganic ions to form ordered mesostructures. Recently, a new family of mesoporous molecular sieves designed as M41S has been discovered.[105] A liquid crystal templating mechanism in which surfactant liquid crystal structures serve as organic templates has been proposed for the formation of these materials.[105,106]

To the microporous materials with pore diameters ≤ ∼20 Å belong, among others, aluminophosphate ($AlPO_{4-n}$) and silicoaluminophosphate (SAPO-*n*) molecular sieves. The SAPO-11 molecular sieve is composed of 4-, 6-, and 10-ring channels, interconnected by 6-ring windows, a structure also found for $AlPO_4$-11, except that in SAPO-11 the framework phosphorous tetrahedral sites are partially substituted by silicon. This substitution (P^{5+}/Si^{4+}) produces a net negative framework charge which is balanced by H^+ ions which can be ion exchanged. The modification of these materials by isomorphous replace-

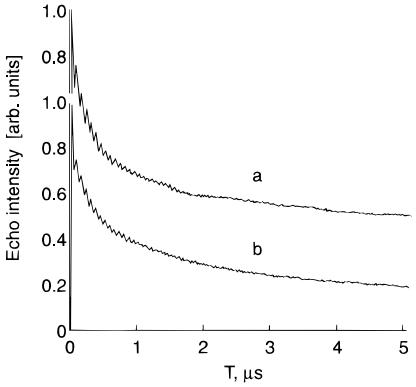

Figure 33. Three-pulse ESEEM patterns for Cu(II)-doped mesoporous hectorite (a) after air-drying and (b) evacuation at room temperature. Only ^{1}H modulation is observed (see text). (Reprinted from ref 107. Copyright 1995 American Chemical Society.)

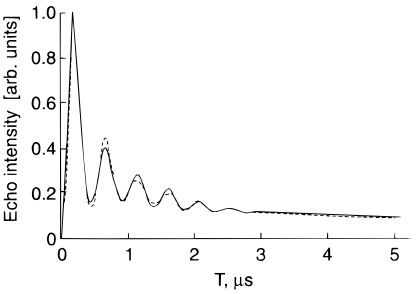

Figure 34. Three-pulse ESEEM patterns for Cu−MP−hect with adsorbed D_2O. Solid and dotted lines indicate experimental and simulated spectra, respectively. (Reprinted from ref 107. Copyright 1995 American Chemical Society.)

ment of framework atoms by TMIs or by direct incorporation of such ions into framework positions is of potential significance for specific catalytic reactions. The catalytic activity of such materials depends on the oxidation state, location, and dispersion of TMIs and the properties of the supporting molecular sieve.

Yamada and co-workers[107] investigated recently, by means of EPR and ESEEM, Cu(II)-doped mesoporous materials (Cu−MP−hect) produced by calcination of organophilic silica-bearing hectorite. After air-drying and vacuum-drying an anisotropic EPR spectrum of Cu−MP−hect is obtained, indicating that the Cu(II) species is bound to the interlayer surface or to the pillars. The lattice of hectorite is composed of silicon, magnesium, and lithium, the two latter elements being distributed in the central octahedral sheet of a layer. The ESEEM pattern of an air-dried sample (Figure 33) does not show any ^{7}Li modulation, suggesting that the Cu(II) species is not located at a Li site in the octahedral sheet but at a site close to the pillar. In the ESEEM spectrum, a distinct modulation related to the interaction with H is obtained at $\tau = 0.09$ μs. After equilibration with deuterated water, a strong ESEEM signal is obtained (Figure 34) which is best simulated, using a two-shell model with N (number of interacting nuclei) = 6, R (distance) = 2.9 Å, and A (isotropic hf interaction) = 0.16 MHz in one shell and $N = 2$, $R = 3.7$ Å, and $A = 0.04$ MHz in the other shell. The Cu−D distance of 2.9 Å is characteristic of direct coordination of D_2O to Cu(II). Thus, three water molecules are directly coordinated to the Cu(II) cations and another water molecule is more weakly coordinated at a further distance.

The ESEEM signal for a Cu−MP−hect sample with adsorbed CD_3OH fits best a two shell model. The experimental spectrum corresponds well to $N = 3$, $R = 3.8$ Å, and $A = 0.07$ MHz in one shell and $N = 3$, $R = 4.8$ Å, and $A = 0$ MHz in the other shell. These data indicate that in Cu−MP−hect, the Cu(II) cations have only one directly coordinated methanol molecule and another one coordinated indirectly.

A series of papers by Kevan and co-workers[108−110] deal with location and properties of Ni^+ ions in microporous materials SAPO-5,11. ^{31}P and ^{27}Al electron spin echo envelope modulations were used to determine location of Ni^+ in the NiH−SAPO-11 matrix at various dehydration states. The location site changes with temperature of dehydration. Interaction of Ni^+ with adsorbates, water, methanol, and ethylene, was evidenced by ESEEM spectra. The molecular structure of the species created in the course of adsorption was proposed.

The location and coordination of silver clusters and silver−alcohol adducts stabilized in SAPO molecular sieves were extensively studied by Kevan and co-workers[111] using EPR and ESEEM techniques. These studies were related to previous research work of this group on silver atoms produced in Ag^+-exchanged montmorillonite (smectite)[112] or in zeolites.[113] Similar studies were performed on Pd(I) in K- and L-zeolites[114] and in SAPO molecular sieves.[115]

The main advantage of time-resolved EPR techniques is the possibility to extract important information concerning the nearest neighbors of the TMIs, their location on the surface or in framework position, number of coordinated ligands and their distance from the coordinating metal ion, mobility and dispersion of TMIs. All these pieces of information may be obtained from even very weak shf interactions which are usually not seen in conventional EPR spectra.

VII. Concluding Remarks

The joint application of coordination chemistry principles and EPR techniques appears very useful in studying phenomena occurring at oxide surfaces. EPR spectroscopy can allow one to distinguish features originating from various surface centers, to identify them, and to follow their transformations upon interaction with gas (liquid)−phase molecules. The application of the coordination chemistry concepts to oxide-supported TMIs has led us to describe and improve our understanding of the processes taking place on oxide surfaces in terms of exchange, elimination, or coordination of ligands. The mechanism of these processes may be deduced, by analyzing the evolution of the EPR spectra as a function of parameters such as temperature, pressure, or concentration of reagents and time.

Overall, the EPR techniques have largely contributed to the emergence of a new field, the so-called interfacial coordination chemistry.[116]

VIII. Acknowledgments

The authors are very grateful to Dr. Zbigniew Sojka (Jagiellonian University, Cracow) for valuable dis-

cussions. K.D. is very much obliged to the Université Pierre et Marie Curie, Paris, for several invitations to stay as Professeur Invité at the Laboratoire de Réactivité de Surface which enabled her to work on this review.

IX. References

(1) Werner, A. *Z. Anorg. Chem.* **1893**, *3*, 267.
(2) Kauffman, Ed. *Am. Chem. Soc. Symp. Ser.* **1994**, *565*.
(3) Wilkinson, G. *Comprehensive Coordination Chemistry*; Gillard, R. D., McCleverty, J. E., Eds.; Pergamon Press: Oxford, 1987.
(4) Greenwood, N. N.; Earnshaw, A. *Chemistry of the Elements*; Pergamon: Oxford, 1990.
(5) Purcell, K. F.; Kotz, J. C. *Inorganic Chemistry*; Saunders: Philadelphia, 1977; p 514.
(6) Huheey, J. E. *Inorganic Chemistry*, 2nd ed; Harper & Row: New York, 1978.
(7) Cotton, F. A.; Wilkinson, G. *Advanced Inorganic Chemistry*; 4th Ed.; Wiley: New York, 1980.
(8) Dowden, D. A.; Wells, D. *Actes du Deuxiéme Congrés International de Catalyse*; Technip: Paris, 1960; Part 2, p 1499; see also the general discussion, p 1649.
(9) Che, M. In *Proc. Congr. Catal., Budapest, 1992*; Guczi, L., Solymosi, F., Tétényi, P., Eds.; Elsevier: Amsterdam, 1993; p 31.
(10) Che, M.; Clause, O.; Bonneviot, L. *Proc. 9th Int. Congr. Catal., Calgary*, **1988**, *4*, 1750.
(11) Che, M.; Bonneviot, L. *Z. Phys. Chem. N. F.* **1987**, *152*, 113.
(12) Bonneviot, L.; Legendre, O.; Kermarec, M.; Olivier, D.; Che, M. *J. Colloid Interf. Sci.* **1990,** *134*, 534.
(13) Brindley, G. W.; Brown, G. *Crystal Structures of Clay Minerals and their X-Ray Identification*, 2nd ed.; Mineralogy Society: London, 1980; p 2.
(14) Bonneviot, L.; Clause, O.; Che, M.; Manceau, A.; Dexpert, H. *Catal. Today* **1989**, *6*, 39.
(15) Jørgensen, C. K. *Acta Chem. Scand.* **1956**, *10*, 887.
(16) Jørgensen, C. K. *Struct. Bonding*, **1966**, *1*, 234.
(17) Jørgensen, C. K. *Acta Chem. Scand.* **1955**, *9*, 116, 1362.
(18) Jørgensen, C. K. *Inorganic Complexes*; Academic Press: New York, 1963; p 54.
(19) Jørgensen, C. K. *Absorption Spectra and Chemical Bonding in Complexes*; Pergamon: Elmsford, 1962.
(20) Bergaoui, L.; Lambert, J.-F.; Suquet, H.; Che, M. *J. Phys. Chem.* **1995**, *99*, 2155.
(21) Che, M.; Lambert, J.-F.; Bozon-Verduraz, F. In press.
(22) Iler, R. K. *The Chemistry of Silica*; Wiley: New York, 1979; p 63.
(23) Brunelle, J. P. *Pure Appl. Chem.* **1978**, *50*, 1211.
(24) Clause, O.; Kermarec, M.; Bonneviot, L.; Villain, F.; Che, M. *J. Am. Chem. Soc.* **1992**, *114*, 4709.
(25) Brinker, C. J.; Scherer, G. *W. Sol-Gel Science*; Academic Press: New York, 1990; p 26.
(26) Davidson, A.; Che, M. *J. Phys. Chem.* **1992**, *96*, 9909.
(27) Che, M.; Tench, A. J. *Adv. Catal.* **1982,** *31*, 77.
(28) Che, M. in *Adsorption and Catalysis on Oxide Surfaces*; Che, M., Bond, G. C., Eds.; Elsevier: Amsterdam, 1985; p 30.
(29) Che, M.; Dyrek, K.; Louis, C. *J. Phys. Chem.* **1985**, *89*, 4526.
(30) Che, M.; Conesa B.; Gonzalez-Elipe, A. R. *J. Phys. Chem.* **1986**, *90*, 618.
(31) Giamello, E.; Sojka, Z.; Che, M.; Zecchina, A. *J. Phys. Chem.* **1986**, *90*, 6084.
(32) Sojka, Z.; Giamello, E.; Che, M.; Zecchina, A.; Dyrek, K. *J. Phys. Chem.* **1988**, *92*, 1541.
(33) Che, M.; Bonneviot, L. *Pure Appl. Chem.* **1988**, *60*, 1369.
(34) Haber, J. *Proc. 8th Int. Congr. Catal., Berlin*, **1984**, *1*, 85.
(35) Che, M.; Shul, Y. G. *Science and Technology in Catalysis*; Kodansha: Tokyo, 1995, p 21.
(36) Che, M.; Védrine, J.; Naccache, C. *J. Chim. Phys.* **1969,** *66*, 579.
(37) Che, M.; Giamello, E. *in Spectroscopic Characterization of Heterogeneous Catalysts*; Fierro, J. L. G., Ed.; Elsevier: Amsterdam, 1993; Vol. 57b, p 265B. (Note: There was an inversion of captions between Figures 5.9 and 5.10.)
(38) Lozos, G. P.; Hoffmann, B. M.; Franz, G. C. *QCPE* **1973,** 265.
(39) (a) Bonneviot, L.; Olivier, D.; Che, M. *J. Mol. Catal.* **1983**, *21*, 415. (b) Bonneviot, L. Thesis, Université P. et M. Curie, Paris, 1983.
(40) Louis, C.; Che, M. *J. Phys. Chem.* **1987**, *91*, 2875.
(41) Che, M.; Giamello, E. in *Catalyst Characterization: Physical Techniques for Solid Materials*; Imelik, B., Védrine, J. C., Eds.; Plenum Press: New York, 1994; p 131.
(42) Lunsford, J. H.; Vansant, E. F. *J. Chem. Soc., Faraday Trans. 2* **1973**, *69*, 1028.
(43) Che, M.; McAteer, J. C.; Tench, A. J. *J. Chem. Soc., Faraday Trans. 1* **1978**, *74*, 2378.
(44) Sperlich, G.; Urban, P.; Frank, G. *Z. Phys.* **1973**, *263*, 315.
(45) Hyde, J. S.; Pasenkiewicz-Gierula, M.; Basosi, R.; Froncisz, W.; Antholine, W. E. *J. Magn. Reson.* **1989**, *82*, 63.
(46) Froncisz W.; Hyde, J. S. *J. Chem. Phys.* **1980**, *73*, 3123.
(47) Schlick, S.; Alonso-Amigo, M. G.; Bednarek, J. *Colloids Surf. A* **1993**, *72*, 1.
(48) Goodman, B. A.; Raynor, J. B. *Adv. Inorg. Chem. Radiochem.* **1970**, *13*, 135.
(49) Dyrek, K.; Labanowska, M. *J. Chem. Soc., Faraday Trans. 1* **1991**, *87*, 1003.
(50) Dyrek, K.; Rokosz, A.; Madej, A. *Appl. Magn. Res.* **1994**, *6*, 309.
(51) Dyrek, K.; Madej, A.; Mazur, E.; Rokosz, A. *Colloids Surf.* **1990**, *45*, 135.
(52) Chang, T.-T. *Magn. Res. Rev.* **1984,** *9***,** 65.
(53) Peacock, I. M.; Sharp, M. J.; Parker, A. J.; Ashmore, P. G.; Hockey, J. A. *J. Catal.* **1969**, *15*, 379.
(54) Bielañski, A.; Dyrek, K.; Serwicka, E. *J. Catal.* **1980**, *66*, 316.
(55) Dyrek, K.; Labanowska, M. *J. Catal.* **1983**, *81*, 46.
(56) Dyrek, K.; Labanowska, M. *J. Catal.* **1985**, *96*, 32.
(57) Dyrek, K.; Sojka, Z. *J. Chem. Soc. Faraday Trans. 1* **1982**, *78*, 3177.
(58) Sojka, Z.; Dyrek, K.; Roberge, P. C.; Che, M. *Polish J. Chem.* **1991**, *65*, 637.
(59) Dyrek, K.; Kruczala, K.; Schlick, S.; Sojka, Z. *J. Phys. Chem.* **1993**, *97*, 9196.
(60) Che, M.; Fournier, M.; Launay, J. P. *J. Chem. Phys.* **1979,** *71*, 1954.
(61) Manoharan, P. T.; Rogers, M. T. *J. Chem. Phys.* **1968**, *49*, 5510.
(62) Barry, T. I.; Lay, L. A. *J. Phys. Chem. Solids* **1968**, *29*, 1395.
(63) Che, M.; Tench, A. J. *Adv. Catal.* **1983**, *32*, 1.
(64) Naccache, C.; Che, M.; Ben Taarit, Y. *Chem. Phys. Lett.* **1972**, *13*, 109.
(65) Chao, C. C.; Lunsford, J. H. *J. Phys. Chem.* **1972**, *76*, 1546.
(66) Shvets, V. A.; Sarichev, M. E.; Kazansky, V. B. *J. Catal.* **1968**, *11*, 378.
(67) Mériaudeau, P.; Ben Taarit, Y. In *Magnetic Resonance in Colloid and Interface Science*; Fraissard, J. P., Resing, H. A., Eds.; Dordrecht: The Netherlands, 1980; p 29.
(68) De Armond, K.; Garret, B. B.; Gutowsky, H. S. *J. Chem. Phys.* **1965**, *42*, 1019.
(69) Che, M.; Louis, C.; Sojka, Z. *J. Chem. Soc., Faraday Trans. 1* **1989**, *85*, 3939.
(70) Sojka, Z.; Che, M. *J. Phys. Chem.* **1995**, *99*, 5418.
(71) Louis, C.; Che, M. *J. Catal.* **1992**, *135*, 156.
(72) Mc Clure, D. S. *J. Chem. Phys.* **1949**, *17*, 905.
(73) Che, M.; Tench, A. J. *Chem. Phys. Lett.* **1973**, *18*, 199.
(74) Louis, C.; Lepetit, C.; Che, M. *Mol. Eng.* **1994**, *4*, 3.
(75) Louis, C.; Tatibouët, J.-M.; Che, M. *J. Catal.* **1988**, *109*, 354.
(76) Bonneviot, L.; Che, M.; Dyrek, K.; Schöllner, R.; Wendt, G. *J. Phys. Chem.* **1986**, *90*, 2379.
(77) Chien, S.-H.; Shao, L.-Y.; Che, M.; Bonneviot, L. *Solid State Ionics* **1989,** *32/33*, 962.
(78) Naccache, C.; Ben Taarit, Y. *Chem. Phys. Lett.* **1971**, *11*, 11.
(79) Nicula, A.; Stamires, D.; Turkevich, J. *J. Chem. Phys.* **1965**, *42*, 3684.
(80) Dyrek, K.; Sojka, Z. in *Adsorption and Catalysis on Oxide Surfaces*; Che, M., Bond, G. C., Eds.; Elsevier: Amsterdam, 1985; p 195.
(81) Coluccia, S.; Barton, A.; Tench, A. J. *J. Chem. Soc., Faraday Trans. 1* **1981**, *77*, 2203.
(82) Che, M.; Dyrek, K.; Louis, C. *J. Phys. Chem.* **1985**, *89*, 4531.
(83) Indovina, V.; Cordischi, D. *J. Chem. Soc., Faraday Trans. 1* **1982**, *78*, 1705.
(84) Howe, R. F.; Lunsford, J. H. *J. Am. Chem. Soc.* **1975**, *97*, 5156.
(85) Che, M.; McAteer, J. C.; Tench, A. J. *Chem. Phys. Lett.* **1975**, *31*, 145.
(86) Bogdanovic, B. *Adv. Organomet. Chem.* **1979**, *17*, 105.
(87) Cai, F. X.; Lepetit C.; Kermarec, M.; Olivier, D. *J. Mol. Catal.* **1987**, *43*, 93.
(88) Parshall, G. W. *Homogeneous Catalysis*; Wiley: New York, 1980.
(89) Lepetit, C.; Kermarec, M.; Olivier, D. *J. Mol. Catal.* **1989**, *51*, 95.
(90) Tatibouët, J.-M.; Germain, J. E. *J. Catal.* **1981**, *72*, 375.
(91) Volta J. C.; Portefaix, J. L. *Appl. Catal.* **1985**, *18*, 1.
(92) Rocchiccioli-Deltcheff, C.; Amirouche, M.; Hervé, G.; Fournier, M.; Che, M.; Tatibouët, J. M. *J. Catal.* **1990**, *126*, 591.
(93) Freed J. H. *Annu. Rev. Phys. Chem.* **1972**, *23*, 265.
(94) Shiotani, M.; Moro, G.; Freed, J. H. *J. Chem. Phys.* **1981**, *74*, 2616.
(95) Kazuyuki, T.; Shiotani, M.; Freed, J. H. *J. Phys. Chem.* **1983**, *87*, 3425.
(96) Kazusaka, A.; Yong, L. K.; Howe, R. F. *Chem. Phys. Lett.* **1978**, *57*, 592.
(97) Barzaghi, M.; Beringhelli, T.; Morazzoni, F. *J. Mol. Catal.* **1982**, *14*, 357.
(98) Antoniu, A. A. *J. Phys. Chem.* **1964**, *68*, 2754.
(99) Bassetti, V.; Burlamacchi, L.; Martini, G. *J. Am. Chem. Soc.* **1979**, *101*, 5471.
(100) Iler, R. K. *The Chemistry of Silica*; Wiley & Sons, Inc.: New York, 1979.
(101) Wefers, K.; Misra, C. Oxides and Hydroxides of Aluminum; Alcoa Technical Paper No. 19, Revised; Alcoa Laboratories: 1987.
(102) Pinnavaia, T. J. *Science* **1983**, *220*, 365.
(103) Vaughan, D. E. W. *ACS Symp. Ser.* **1988**, *368*, 308.

(104) Tindwa, R. M.; Ellis, D. K.; Peng, G. Z.; Clearfield, A. *J. Chem. Soc., Faraday Trans. 1* **1985**, *81*, 545.
(105) Kresge, C. T.; Leonowicz, M. E.; Roth, W. J.; Vartuli, J. C.; Beck, J. S. *Nature* **1992**, *359*, 710.
(106) Beck, J. S.; Vartuli, J. C.; Roth, W. J.; Leonowicz, M. E.; Kresge, C. T.; Schmitt, K. D.; Chu, C. T-W.; Olson, D. H.; Sheppard, E. W.; McCullen, S. B.; Higgins, J. B.; Schlenker, J. L. *J. Am. Chem. Soc.* **1992,** *114*, 10834.
(107) Yamada, H.; Azuma, N.; Kevan, L. *J. Phys. Chem.* **1995**, *99*, 11190.
(108) Azuma, N.; Kevan, L. *J. Phys. Chem.* **1995**, *99*, 5083.
(109) Azuma, N.; Hartmann, M.; Kevan, L. *J. Phys. Chem.* **1995**, *99*, 6670.
(110) Hartmann, M.; Azuma, N.; Kevan, L. *J. Phys. Chem.* **1995**, *99*, 10988.
(111) Michalik, J.; Azuma, N.; Sadlo, J.; Kevan, L. *J. Phys. Chem.* **1995**, *99*, 4679.
(112) Brown, D. R.; Luca, V.; Kevan, L. *J. Chem. Soc., Faraday Trans.* **1991**, *87*, 2749.
(113) Brown, D. R.; Kevan, L. *J. Phys. Chem.* **1986**, *90*, 1129.
(114) Yu, J. S.; Kevan, L. *Langmuir* **1995**, *11*, 1617.
(115) Yu, J. S.; Comets, J. M.; Kevan, L. *J. Phys. Chem.* **1993**, *97*, 10433.
(116) Lepetit, C.; Che, M. *J. Mol. Catal.* **1995**, *100*, 147.

CR950259D